

ALMA CENSUS OF FAINT 1.2 mm SOURCES DOWN TO 0.02 mJy: EXTRAGALACTIC BACKGROUND LIGHT AND DUST-POOR HIGH-Z GALAXIES

SEIJI FUJIMOTO¹, MASAMI OUCHI^{1,2}, YOSHIKI ONO¹, TAKATOSHI SHIBUYA¹,
MASAFUMI ISHIGAKI¹, HIROSHI NAGAI³, AND RIEKO MOMOSE³

ApJS in press

ABSTRACT

We present statistics of 133 faint 1.2-mm continuum sources detected in about 120 deep ALMA pointing data that include all the archival deep data available by 2015 June. We derive number counts of 1.2 mm continuum sources down to 0.02 mJy partly with the assistance of gravitational lensing, and find that the total integrated 1.2 mm flux of the securely identified sources is $22.9^{+6.7}_{-5.6}$ Jy deg⁻² that corresponds to 104^{+31}_{-25} % of the extragalactic background light (EBL) measured by COBE observations. These results suggest that the major 1.2 mm EBL contributors are sources with 0.02 mJy, and that very faint 1.2 mm sources with $\lesssim 0.02$ mJy contribute negligibly to the EBL with the possible flattening and/or truncation of number counts in this very faint flux regime. To understand the physical origin of our faint ALMA sources, we measure the galaxy bias b_g by the counts-in-cells technique, and place a stringent upper limit of $b_g < 3.5$ that is not similar to b_g values of massive DRGs and SMGs but comparable to those of UV-bright sBzKs and LBGs. Moreover, in optical and near-infrared (NIR) deep fields, we identify optical-NIR counterparts for 59% of our faint ALMA sources, majority of which have luminosities, colors, and the IRX- β relation same as sBzKs and LBGs. We thus conclude that about a half of our faint ALMA sources are dust-poor high- z galaxies as known as sBzKs and LBGs in optical studies, and that these faint ALMA sources are not miniature (U)LIRGs simply scaled down with the infrared brightness.

Keywords: galaxies: formation — galaxies: evolution — galaxies: high-redshift

1. INTRODUCTION

Since the infrared (IR) extragalactic background light (EBL) was first identified by the *Cosmic Background Explorer* (COBE) satellite, it has been known that the total energy of IR EBL is comparable to that of the optical EBL (Puget et al. 1996; Fixsen et al. 1998; Hauser et al. 1998; Hauser & Dwek 2001; Dole et al. 2006). Because dusty star-forming galaxies at high redshift should significantly contribute to the IR EBL, the IR EBL is key to understanding the dusty-side of the cosmic star formation history and to constraining physical parameters of galaxy formation models (e.g., Granato et al. 2004; Baugh et al. 2005; Fontanot et al. 2007; Shimizu et al. 2012; Hayward et al. 2013).

To reveal the origin of the IR EBL, we need reliable number counts from bright to faint flux limits. The IR EBL of the low-frequency end, at submillimeter (submm) and millimeter (mm) wavelengths, is one of the most advantageous wavelength regimes, due to the negative k -correction. Previous blank field observations with single dish telescopes have revealed that the bright dusty high- z objects of submillimeter galaxies (SMGs; Lagache et al. 2005) are not major contributors of the EBL. SCUBA and LABOCA observations have resolved 20 – 40% of the EBL at submm wavelength (e.g., Eales et al. 2000; Smail et al. 2002; Coppin et al.

2006; Knudsen et al. 2008; Weiß et al. 2009). Similar results have been obtained by AzTEC observations that they have resolved 10 – 20% of the EBL at mm wavelength (e.g., Perera et al. 2008; Hatsukade et al. 2011; Scott et al. 2012). These observations suggest that there should exist high- z populations different from SMGs, and that such populations are major EBL contributors in submm and mm wavelengths.

There are two observational challenges for fully resolving the EBL. First is the spatial resolution. The poor spatial resolution of the single-dish observations causes the serious source confusion (Condon 1974) that skews the observed number counts. Second is the sensitivity. Most of the submm and mm telescopes reach the limiting fluxes of ~ 1 mJy that correspond to the flux range of the SMGs. To detect submm sources fainter than ~ 1 mJy, there are many efforts (e.g., Smail et al. 2002; Chapman et al. 2002; Knudsen et al. 2008; Johansson et al. 2011; Chen et al. 2013). Knudsen et al. (2008) and Chen et al. (2013) observe massive galaxy clusters at 850 μ m for gravitationally lensed sources, and resolved 50%–180% of the EBL down to the intrinsic flux of $S_{850 \mu\text{m}} > 0.1$ mJy. These results indicate that there exist faint (< 1 mJy) populations significantly contributing to the EBL (e.g., Smail et al. 2002; Knudsen et al. 2008). However, large uncertainties of the measurements still remain, due to the source blending and cosmic variance. Moreover, the physical origin of these faint submm and mm sources is unknown.

The Atacama Large Millimeter / submillimeter Array (ALMA) enables us to investigate the faint submm and mm sources with the negligibly small uncertainties of the

sfseiji@icrr.u-tokyo.ac.jp

¹ Institute for Cosmic Ray Research, The University of Tokyo, Kashiwa, Chiba 277-8582, Japan

² Kavli Institute for the Physics and Mathematics of the Universe (Kavli IPMU), WPI, The University of Tokyo, Kashiwa, Chiba 277-8583, Japan

³ National Astronomical Observatory of Japan, Mitaka, Tokyo 181-8588, Japan

source confusion and blending, having its capabilities of high angular resolution and sensitivity. The first ALMA mm search for faint sources below $S_{1\text{mm}} \sim 1.0$ mJy with no lensing effect has been conducted by Hatsukade et al. (2013). The study reports that they resolve $\sim 80\%$ of the EBL down to $S_{1\text{mm}} = 0.1$ mJy in 20 targets residing in one blank field of the Subaru/XMM-Newton Deep Survey (SXDS; Furusawa et al. 2008). Due to the single field observations, this result would include unknown effects of cosmic variance. Subsequently, using multi-field deep ALMA 1mm maps of Bands 6 and 7 down to the flux limit of $S_{1\text{mm}} = 0.1$ mJy, Ono et al. (2014) and Carniani et al. (2015) have claimed an EBL resolved fraction of $\sim 60\%$ that is smaller than the one of Hatsukade et al. (2013). The uncertainties from cosmic variance are probably reduced with the multi-field data. Including the effects of the cosmic variance, only about a half of the EBL has been resolved with the present ALMA flux limit of $S_{1\text{mm}} = 0.1$ mJy.

There is another remaining issue about the IR EBL. Although these studies newly identify faint ALMA sources ($S_{1\text{mm}} < 1.0$ mJy) contributing to the half of the IR EBL, these studies do not clearly answer to the question about the connection between the faint ALMA sources and optically selected high- z galaxies. Recent observations with *Herschel* have revealed that typical UV-selected galaxies such as Lyman-break galaxies (LBGs) have a median total (8-1000 μm) luminosity of $L_{\text{IR}} \simeq 2.2 \times 10^{11} L_{\odot}$ (Reddy et al. 2012; Lee et al. 2012; Davies et al. 2013). The stacking analysis of *Herschel* and ALMA data has also shown that K -selected galaxies, including star-forming BzK galaxies (sBzKs), have total IR luminosities of $L_{\text{IR}} = (5 - 11) \times 10^{11} L_{\odot}$ (Decarli et al. 2014). These ranges of the IR luminosities of LBGs and sBzKs correspond to the mm flux of $S_{1\text{mm}} \sim 0.1 - 1$ mJy if we assume a modified black body with $\beta_d = 1.8$, dust temperature $T_d = 35\text{K}$, and a source redshift $z = 2.5$. This mm flux range is similar to the one of the faint ALMA sources, implying that these sources could be mm counterparts of the optically selected galaxies.

There is another approach for characterizing the faint ALMA sources. Because the spatial distribution of galaxies is related to the underlying distribution of dark haloes in the standard scenario of structure formation in ΛCDM universe, the clustering analysis is a powerful tool for understanding the connection between various galaxy populations. Clustering analyses have been carried out over the past decade for bright SMGs observed with single-dish telescopes, and concluded that the clustering amplitudes, or galaxy biases, are large, and that the hosting dark halo masses of the bright SMGs are estimated to be $\sim 10^{13} M_{\odot}$ (Webb et al. 2003; Blain et al. 2004; Weiß et al. 2009; Williams et al. 2011; Hickox et al. 2012, cf. Miller et al. 2015). On the other hand, however, the dark halo properties of the faint ALMA sources are poorly known, except for the result of Ono et al. (2014) who have obtained, for the first time, a meaningful constraint on a galaxy bias, $b_g \leq 4$, for faint ALMA sources. In this way, the faint ALMA sources are not well studied. To understand the physical origin of faint ALMA sources, one should study faint ALMA sources with a more complete data set on the basis of

individual sources as well as statistics.

In this paper, we analyze the large dataset of multi-field deep ALMA data including the complete deep datasets archived by 2015 June. Sixty-six independent-field and one cluster maps are taken by ~ 120 ALMA pointings in Band 6/7 to reveal the origins of the EBL and faint ALMA sources in mm wavelength. Note that this is the first step for statistically investigating faint sources behind a lensing cluster with ALMA. The structure of this paper is as follows. In Section 2, we describe the observations and the data reduction. Section 3 outlines the method of the source extraction, our simulations for deriving the number counts, and the mass model development for the cluster. We compare the number counts from our and previous studies, and estimate the resolved fraction of the EBL at 1.2 mm in section 4. In Section 5, we report the results of the clustering analysis for our faint ALMA sources. We investigate optical-NIR counterparts of our faint ALMA sources in Section 6. The summary of this study is presented in Section 7.

Throughout this paper, we assume a flat universe with $\Omega_m = 0.3$, $\Omega_{\Lambda} = 0.7$, $\sigma_8 = 0.8$, and $H_0 = 70 \text{ km s}^{-1} \text{ Mpc}^{-1}$. We use magnitudes in the AB system (Oke & Gunn 1983).

2. DATA AND REDUCTION

We use 67 continuum maps obtained by ~ 120 pointing of the ALMA cycle 0-2 observations in Band 6/7 that accomplish high sensitivities and angular resolutions. Tables 1 and 2 present the summary and the detailed properties, respectively, for these 67 continuum maps. We define sub-datasets by the mapping modes and the depths because these two conditions would make different systematics. For the mapping mode definitions, there are maps targeting field regions by single pointing observations, referred to as 'field' data, 4 and 62 out of which are taken from our programs and the ALMA archive, respectively. One map for a galaxy cluster taken by mapping observations, referred to as 'cluster' data, is from the ALMA archive.

For the depth definitions, we divide these 66 maps of 'field' data into two sub-datasets with low ($\leq 60 \mu\text{Jy}$) and high ($> 60 \mu\text{Jy}$) noise levels, which we refer to as 'deep' and 'medium-deep' data, respectively. This is because the short-integration data would have more chances to contain systematic noise. As shown in Table 2, we use the sub-dataset names of A and B for the deep and medium-deep field data, respectively. The sub-dataset name of the deep cluster data is C.

In this section, we describe the details of these 67 continuum maps of 'deep', 'medium-deep', and 'cluster' data, and present our reduction procedures.

2.1. Our Data

The 4 maps of the field data were obtained by our ALMA single pointing observations. Two out of the four maps were taken in the ALMA cycle-0 Band 6 observations for the spectroscopically confirmed Ly α emitter (LAE) at $z = 6.595$, Himiko (Ouchi et al. 2013) and an LAE at $z = 6.511$, NB921-N-79144 (Ouchi et al. 2010, PI R. Momose). See Ono et al. (2014) for the summary of these observations. We also utilize two maps of newly obtained (ALMA cycle 2) field data of Bands 6 and 7 taken

Table 1
Data Summary

Sub-Dataset (1)	Number of Maps (2)
Deep data (A)	41
Medium-deep data (B)	25
Cluster data (C)	1

Note. — The sub-dataset names of A, B, and C are written in parenthesis. (1): ALMA maps with low ($\leq 60 \mu\text{Jy}$) and high ($> 60 \mu\text{Jy}$) noise levels are referred to as Deep and Medium-deep data, respectively. (2): Number of the ALMA maps in each sub-dataset.

for spectroscopically confirmed LAEs at $z = 5.7$ (NB816-S-61269; Ouchi et al. 2008) and at $z = 7.3$ (NB101-S-2904; Konno et al. 2014, Ouchi et al. in preparation). The NB816-S-61269 observations were carried out in the ALMA program of #2012.1.00602.S (PI: R. Momose) on 2014 May 20, Jun 19, and July 7 with 43 12-m antennae array in the range of 18 – 650 m baseline. The full width at half maximum (FWHM) of the primary beam was $20''.6$. The available 7.5 GHz bandwidth with four spectral windows was centered at an observed frequency of 290.8 GHz (i.e. ~ 1.03 mm). J0217+0144 and J2258-279 were observed as a flux calibrator, while J0006-0623 was used for bandpass calibrator. Phase calibration was generally performed by using observations of J0217+0144 and J0215-0222. The total on-source observed time was ~ 2.3 hours. The NB101-S-2904 data were taken in the ALMA program of #2012.1.00088.S (PI: M. Ouchi) on 2014 July 22, August 6, 7, 14, and 18, with 55 12-m antennae array in the extended configuration of 18-1300 m baseline. The full width at half maximum (FWHM) of the primary beam was $25''.3$. The center of the observed frequency is 237.9 GHz (i.e. ~ 1.26 mm). J0238+166, J2258-279, and J0334-401 were used for primary flux calibrators. Bandpass and phase calibrations were performed with J0241-0815/J0238+1636 and J0215-0222/J0217+0144, respectively. The total on-source integration time was ~ 5.2 hours.

2.2. Archival Data

To increase the number of ALMA sources, we make full use of ALMA archival data of cycles 0 and 1 that became public by 2015 June. We select all of the available ALMA Band 6/7 data sets fulfilling the following three criteria: 1) The 1σ noise level is $\lesssim 100 \mu\text{Jy}/\text{beam}$ for the continuum maps, 2) No bright ($\geq 50\sigma$) sources like AGN, QSO and SMG are included in the maps, and 3) The galactic latitude is high enough to avoid Galactic objects. The second criterion is important to reduce the chance for selecting residual side lobes of the bright sources that might remain even after the CLEAN algorithm on Common Astronomy Software Applications (CASA; McMullin et al. 2007) package. Moreover, the second criterion significantly reduces the systematic uncertainties from galaxy clustering because it is reported that there is a clear excess of submm number counts around bright sources such as AGNs and SMGs (Silva et al. 2015; Simpson et al. 2015a)

2.2.1. Field Data

On the basis of our complete archival data search up to 2015 June with these three criteria, we collect the 62 maps of the field data taken by single-pointing observations: 2 from Willott et al. (2013), 20 from Hatsukade et al. (2013), 1 from Ota et al. (2014), 2 from Hatsukade et al. (2014), 1 from Berger et al. (2014), 3 from Carniani et al. (2015), 20 from ALMA #2012.1.00076, 2 from ALMA #2012.1.00676.S, 2 from ALMA #2012.1.00323, 3 from ALMA #2012.1.00536, 4 from ALMA #2012.1.00934, and 2 from ALMA #2012.1.00610. The ALMA #2012.1.00076 data were taken by PI K. Scott for 20 IR galaxies at $z = 0.25 - 0.65$ in January 2014 with Band 6. The total on-source integration is $\sim 20 - 40$ min for each map. The ALMA #2012.1.00676.S observations were carried out by PI C. Willott for 2 quasars at $z \sim 6$ in the end of November 2013 with Band 6. The total on-source integration is ~ 40 min. The ALMA #2012.1.00323.S observations were performed by PI G. Popping for 2 star-forming galaxies in March 2014 with Band 6. The total on-source integration is ~ 7 min for each source. The ALMA #2012.1.00536.S data were taken by PI C. Martin for 3 LAEs at $z = 5.7$ with Band 7. The total on-source integration is $\sim 20 - 40$ min for each source. The ALMA #2012.1.00934.S observations were conducted by PI B. Phillip for 4 normal star-forming galaxies at $z = 2.23$ in January 2014 with Band 6. The total on-source integration is ~ 6 min for each source. The ALMA #2012.1.00610.S observations were carried out by PI B. Posselt for 2 nearby neutron stars in April and Jun 2014 with Band 6. The total on-source integrations are ~ 30 and 60 mins for each source.

2.2.2. Cluster Data

One-cluster data were taken for Abell 1689 (A1689) in ALMA cycle 0 and 1 observations (PI: J. Richard) of ALMA #2011.0.00319.S and #2012.1.00261.S. These two programs of A1689 included two different frequency settings, high and low tuning modes. The central-observed frequencies were chosen at 231 and 222 GHz (i.e. ~ 1.30 and 1.35 mm) for the high and the low tuning modes, respectively. Thus, a total of four observing sets were conducted for A1689 through ALMA cycle 0 and 1. Each observing set comprises 2 – 4 sub-blocks of observations in which the source integration time is $\sim 10 - 30$ minutes to make a mosaic map covering the highly magnified area of A1689 by ~ 50 pointings. The first observation set was obtained on 2012 June 17-18, and July 3-4 with 20 antennas in the high-tuning mode.

Mars and Titan were observed as flux calibrators. The bandpass and phase calibrations were performed using observations of 3C 279. The second observation set was taken on 2012 July 14, 15, 28, August 9, and 2013 January 1 with 24 antennas in the low-tuning mode. The available 7.5 GHz bandwidth with four spectral windows was centered at an observed frequency of 222 GHz (i.e. ~ 1.35 mm). Titan was observed as a flux calibrator. Bandpass and phase calibrations were performed with 3C 279. The third observation set was obtained on 2014 March 11 and April 4 with 34 antennas in the low-tuning mode. Titan was observed as a flux calibrator. Bandpass and phase calibrations were carried out with J1256-0547. The fourth observing set was performed on 2014 March 22 and April 4 with 37 antennas in the high-tuning mode.

FUJIMOTO ET AL.
Table 2
 ALMA Maps of this Study

Map ID	Target	λ_{obs} (mm) (1)	ν_{obs} (Band) (GHz) (2)	σ_{cont} ($\mu\text{Jy beam}^{-1}$) (3)	beam size ($'' \times ''$) (4)	$S_{1.2\text{mm}}/S_{\text{obs}}$ (5)	Ref. (6)	Project ID
Deep Data (A)								
1	BDF-3299	1.30	227 (6)	8.5	0.79×0.58	1.28	(a),(b)	2012.A.00040.S 2012.1.00719.S
2	GRB090423	1.35	222 (6)	10.3	0.98×0.75	1.45	(c),(d)	2012.1.00953.S
3	NB101-S-2904	1.26	238 (6)	11.4	0.43×0.33	1.16	(e)	2012.1.00088.S
4	NB816-S-61269	1.03	291 (7)	13.0	0.45×0.42	0.63	(f)	2012.1.00602.S
5	rxj0806	1.31	229 (6)	16.6	0.78×0.63	1.31	(g)	2012.1.00610.S
6	Himiko	1.16	259 (6)	17.0	0.81×0.56	0.90	(h),(i)	2011.0.00115.S
7	BDF-521	1.30	230 (6)	17.7	0.68×0.51	1.28	(a),(b)	2012.1.00719.S
8	IOK-1	1.29	232 (6)	18.8	1.08×0.78	1.25	(j),(k)	2011.0.00767.S
9	rxj2143	1.26	238 (6)	20.8	0.60×0.43	1.16	(l)	2012.1.00610.S
10	CFHQSJ2329-0301	1.20	250 (6)	21.0	0.73×0.63	1.00	(m),(n)	2011.0.00243.S
11	SDF-46975	1.22	244 (6)	21.2	1.23×0.98	1.05	(o),(b)	2012.1.00719.S
12	ID239	1.29	232 (6)	21.7	1.88×0.90	1.25	...	2012.1.00076.S
13	GRB020819B	1.18	254 (6)	22.6	0.91×0.72	0.95	(p)	2011.0.00232.S
14	CFHQSJ0055+0146	1.09	273 (6)	23.3	0.69×0.55	0.75	(m)	2012.1.00676.S
15	ID182	1.23	244 (6)	23.8	1.33×0.89	1.08	...	2012.1.00076.S
16	ID220	1.23	244 (6)	24.2	1.33×0.88	1.08	...	2012.1.00076.S
17	ID244	1.29	232 (6)	24.1	1.87×0.90	1.25	...	2012.1.00076.S
18	CFHQSJ2229+1457	1.12	266 (6)	24.9	0.79×0.70	0.81	(m)	2012.1.00676.S
19	ID247	1.29	232 (6)	25.1	1.87×0.90	1.25	...	2012.1.00076.S
20	ID209	1.29	232 (6)	25.8	1.23×1.01	1.25	...	2012.1.00076.S
21	CFHQSJ0210-0456	1.20	249 (6)	27.2	0.92×0.61	1.00	(m),(n)	2011.0.00243.S
22	MSDM80+3	1.06	283 (7)	28.4	0.84×0.63	0.69	(q)	2012.1.00536.S
23	GRB051022	1.15	262 (6)	28.6	1.15×0.77	0.88	(p)	2011.0.00232.S
24	ID217	1.23	244 (6)	30.3	1.33×0.93	1.08	...	2012.1.00076.S
25	ID225	1.23	244 (6)	31.6	1.34×0.93	1.08	...	2012.1.00076.S
26	SXDS19723	1.27	236 (6)	38.5	0.83×0.68	1.19	(r),(s)	2011.0.00648.S
27	SXDS28019	1.27	236 (6)	38.9	0.84×0.68	1.19	(r),(s)	2011.0.00648.S
28	SXDS22198	1.27	236 (6)	39.0	0.86×0.68	1.19	(r),(s)	2011.0.00648.S
29	SXDS35572	1.27	236 (6)	39.3	0.84×0.68	1.19	(r),(s)	2011.0.00648.S
30	SXDS103139	1.27	236 (6)	39.7	0.83×0.68	1.19	(r),(s)	2011.0.00648.S
31	NB921-N-79144	1.22	245 (6)	50.1	0.76×0.63	1.05	(h),(f)	2012.1.00602.S
32	SXDS42087	1.30	231 (6)	52.9	0.80×0.66	1.28	(r),(s)	2011.0.00648.S
33	SXDS79307	1.30	231 (6)	53.7	0.80×0.66	1.28	(r),(s)	2011.0.00648.S
34	SXDS31189	1.30	231 (6)	54.4	0.81×0.66	1.28	(r),(s)	2011.0.00648.S
35	MSDM29.5-5	1.06	283 (7)	54.6	0.71×0.53	0.69	(q)	2012.1.00536.S
36	HiZELS-UDS-NBK-8806	1.39	216 (6)	55.0	1.86×0.89	1.58	...	2012.1.00934.S
37	HiZELS-UDS-NBK-11473	1.39	216 (6)	55.3	1.86×0.89	1.58	...	2012.1.00934.S
38	MSDM71-5	1.06	283 (7)	56.1	0.72×0.53	0.69	(q)	2012.1.00536.S
39	HiZELS-UDS-NBK-13486	1.39	216 (6)	56.4	1.86×0.89	1.58	...	2012.1.00934.S
40	HiZELS-UDS-NBK-11961	1.39	216 (6)	58.3	1.86×0.89	1.58	...	2012.1.00934.S
41	ID125	1.09	273 (6)	59.1	1.30×0.73	0.75	...	2012.1.00076.S
Medium-Deep Data (B)								
42	ID098	1.09	273 (6)	60.1	1.30×0.72	0.75	...	2012.1.00076.S
43	ID093	1.09	273 (6)	60.3	1.30×0.72	0.75	...	2012.1.00076.S
44	ID143	1.09	273 (6)	61.7	1.31×0.72	0.75	...	2012.1.00076.S
45	SXDS33244	1.25	240 (6)	67.5	1.04×0.64	1.13	(r),(s)	2011.0.00648.S
46	ID163	1.19	252 (6)	68.2	1.36×0.92	0.97	...	2012.1.00076.S
47	ID204	1.19	252 (6)	69.2	1.24×0.86	0.97	...	2012.1.00076.S
48	SXDS13316	1.23	244 (6)	69.3	0.87×0.64	1.08	(r),(s)	2011.0.00648.S
49	ID158	1.19	252 (6)	69.5	1.35×0.92	0.97	...	2012.1.00076.S
50	ID192	1.19	252 (6)	69.7	1.24×0.86	0.97	...	2012.1.00076.S
51	SXDS59863	1.23	244 (6)	71.6	0.85×0.65	1.08	(r),(s)	2011.0.00648.S
52	ID177	1.13	264 (6)	73.0	1.24×0.86	0.83	...	2012.1.00076.S
53	ID107	1.13	264 (6)	73.8	1.24×0.86	0.83	...	2012.1.00076.S
54	SXDS67002	1.23	244 (6)	74.0	0.88×0.64	1.08	(r),(s)	2011.0.00648.S
55	ID112	1.13	264 (6)	75.4	1.24×0.86	0.83	...	2012.1.00076.S
56	ID117	1.13	264 (6)	75.5	1.24×0.86	0.83	...	2012.1.00076.S
57	SXDS9364	1.23	244 (6)	76.7	0.87×0.64	1.08	(r),(s)	2011.0.00648.S
58	SXDS13015	1.23	244 (6)	81.3	0.85×0.65	1.08	(r),(s)	2011.0.00648.S
59	113083	1.32	226 (6)	82.1	1.18×0.72	1.36	...	2012.1.00323.S
60	SXDS68849	1.25	240 (6)	82.3	0.96×0.65	1.13	(r),(s)	2011.0.00648.S
61	SXDS79518	1.25	240 (6)	83.0	1.02×0.65	1.13	(r),(s)	2011.0.00648.S
62	1374240	1.32	226 (6)	84.6	1.20×0.72	1.36	...	2012.1.00323.S
63	SXDS101746	1.25	240 (6)	86.7	1.13×0.65	1.13	(r),(s)	2011.0.00648.S
64	SXDS110465	1.25	240 (6)	87.6	1.13×0.64	1.13	(r),(s)	2011.0.00648.S
65	SXDS1723	1.25	240 (6)	94.0	1.29×0.64	1.13	(r),(s)	2011.0.00648.S
66	SXDS59914	1.25	240 (6)	95.2	1.20×0.65	1.13	(r),(s)	2011.0.00648.S
Cluster Data (C)								
67	A1689	1.32	231 (6)	38.4-40.6 [†]	0.96×0.74	1.36	(t)	2011.0.00319.S 2012.1.00261.S

Note. — (1): Wavelength in the observed frame. (2): Frequency in the observed frame. (3): One sigma noise measured in each map before primary beam correction. (4): Synthesized beam size of our ALMA maps (weighting = 'natural'). (5): Ratio of the flux density at 1.2 mm, $S_{1.2\text{mm}}$, to the one at the observed wavelength, S_{obs} , that is estimated with the modified blackbody spectrum of $\beta_d = 1.8$, a dust temperature of $T_d = 35\text{K}$, and a redshift of $z = 2.5$. (6): Reference. (a) Vanzella et al. (2011); (b) Maiolino et al. (2015); (c) Tanvir et al. (2012); (d) Berger et al. (2014); (e) Konno et al. (2014); (f) Ouchi et al. (2010); (g) Hablerl et al. (1998); (h) Ouchi et al. (2013); (i) Ono et al. (2014); (j) Iye et al. (2006); (k) Ota et al. (2014); (l) Zampieri et al. (2001); (m) Willott et al. (2010); (n) Willott et al. (2013); (o) Ouchi et al. (2009); (p) Hatsukade et al. (2014); (q) Martin et al. (2006); (r) Yabe et al. (2012); (s) Hatsukade et al. (2013);

Ceres was observed as a flux calibrator. Bandpass and phase calibrations were done with J1256-0547. Throughout these four observing sets, the total on-source integration is ~ 5.5 hour.

2.3. Data Reduction

Basically, the data are reduced with CASA version 4.3.0 in a standard manner with the scripts used for the data reduction provided by the ALMA observatory. In this process, we also use previous CASA versions from 3.4 to 4.2.2, if we find problems in the final image that the noise level is significantly higher than the calibrated products provided by the ALMA observatory, or that there remain striped patterns. Exceptionally for the cycle 0 data with the high noise level or the patterned noise, we use the calibrated data produced by the ALMA observatory. Similarly for the data of ALMA #2011.0.00648.S (PI: Ohta), we use a re-calibrated data provided by Seko et al. because they find that the coordinate of a phase calibrator of #2011.0.00648.S is wrong ($\sim 0''.3$), which causes positional offsets (Seko et al. in preparation; Hatsukade et al. 2015).

Our CASA reduction has three major steps: bad data flagging, bandpass calibration, and gain calibration with flux scaling. In the first step, we remove the data of the shadowed antennas and the edge channels of spectral windows. We also do not use the unreliable data such with jumps or a low phase/amplitude gain. We apply the flaggings that are shown in the scripts, but no additional flaggings. This is because we find that the flaggings in the scripts are good enough for our scientific goals. The second step is the bandpass calibration. After we calibrate the phase time variation on the bandpass calibrator scan, we obtain the bandpass calibration in the phase and amplitude. The final step is the gain calibration. We estimate the time variations of the phase and amplitude on the phase calibrators, and then transfer the calibration to the target source by applying the linear interpolation with the results of the phase calibrators. The water vapor radiometer is used for the correction of the short-time phase variations that cannot be traced by the phase calibrators. We estimate flux scaling factors, using solar-system objects and bright QSOs with the flux models of ‘Butler-JPL-Horizons 2012’ and ALMA Calibrator Source Catalog, respectively. The difference of the opacity between the flux calibrators and the target sources is corrected with the system noise temperature (T_{sys}) measurements. The systematic flux uncertainty is typically 10% in bands 6 and 7 (ALMA proposer’s guide⁴).

We perform Fourier transformation for the original uv -data to create “dirty” maps. The continuum maps are made using all the line free channels of the four spectral windows. We process the maps with the auto CLEAN algorithm down to the depth of 3σ noise levels of the dirty maps, using natural weighting. The final cleaned maps achieve angular resolutions of $0''.45 \times 0''.33 - 1''.88 \times 0''.90$. The sensitivities of these ALMA maps range from 8.5 to $95.2 \mu\text{Jy beam}^{-1}$ before the primary beam corrections.

Because the observations of the cluster data were taken place in 4 different epochs, we recalculate the data

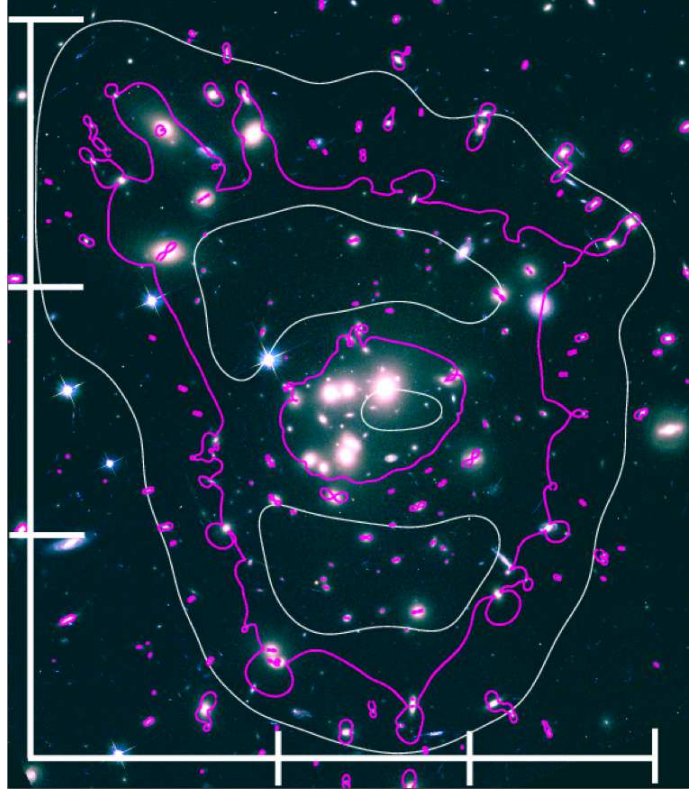


Figure 1. False-color image of A1689 cluster (red: i_{775} , green: V_{625} , red: B_{475}). The critical lines for background sources at $z = 2.5$ are shown with the magenta lines. The white curves are the contours indicating the 50% sensitivity of the deepest part in the mosaic map. The white thick lines and ticks indicate the 9 regions of our noise estimates.

weights with the *statwt* task in CASA based on its visibility scatters which include the effects of integration time, channel width, and systematic temperature. After applying the data weights to the datasets, we combine these two datasets with the *concat* task in CASA. Since the mosaic mapping observations were conducted for the cluster, the noise levels vary by positions. To estimate the noise levels of the cluster data, we divide the cluster’s mosaic map in 9 regions as shown in Figure 1. The data of the 9 regions achieve the 1σ noise levels in the range of 38.4 – $40.6 \mu\text{Jy}$.

3. DATA ANALYSIS

We show our data analyses in the following subsections. The wavelengths of our mm maps fall in the range of $1.03 - 1.32$ mm. Our data set is composed of 63 Band 6 maps and 4 Band 7 maps (Table 2), and the majority of our data are taken with Band 6. Because our major data of the ALMA Band 6 maps have the average wavelength of 1.23 mm, we derive the number counts with a flux density at 1.2 mm, $S_{1.2\text{mm}}$. We scale the flux densities of our mm maps to $S_{1.2\text{mm}}$ with the flux density ratios summarized in Table 2. For the data of the previous studies defined with the wavelengths different from 1.2 mm, we estimate $S_{1.2\text{mm}}$ with the ratios of $S_{1.2\text{mm}}/S_{850\mu\text{m}} = 0.37$, $S_{1.2\text{mm}}/S_{870\mu\text{m}} = 0.39$, $S_{1.2\text{mm}}/S_{1.1\text{mm}} = 0.77$, and $S_{1.2\text{mm}}/S_{1.3\text{mm}} = 1.28$. All of these flux density ratios are calculated based on a modified blackbody whose spectral index β_d and dust temper-

⁴ Section A7: <https://almascience.nao.ac.jp/documents-and-tools/cycle-1/alma-proposers-guide>

ature T_d are similar to those of typical SMGs; $\beta_d = 1.8$ (e.g., Chapin et al. 2009, ; Planck Collaboration 2011) and $T_d = 35$ K (e.g., Kovács et al. 2006; Coppin et al. 2008). Here we assume a source redshift of $z = 2.5$ that is a median redshift value of SMGs (e.g., Chapman et al. 2005; Yun et al. 2012; Simpson et al. 2014).

3.1. Source Detection

We conduct source extraction for our ALMA maps before primary beam corrections with SExtractor version 2.5.0 (Bertin & Arnouts 1996). The source extraction is carried out in high sensitivity regions. For the single-pointing maps presented in Sections 2.1 and 2.2.1, we use the regions with the primary beam sensitivity greater than 50%. For the mosaic map shown in Section 2.2.2, we perform source extraction where the relative sensitivity to the deepest part of the mosaic map is greater than 50%.

We identify sources with a positive peak count above the 3.0σ level, assuming the sources are not resolved out in our ALMA maps. The catalog of these sources is referred to as the 3.0σ -detection catalog. From our 3.0σ -detection catalog, we remove the objects located at the map centers that are main science targets of the archived-data ALMA observations.

3.2. Spurious Sources and Source Catalog

The 3.0σ -detection catalog should include many spurious sources, because the detection is simply determined with a peak pixel count. To evaluate the number of the spurious sources, we conduct negative peak analysis (Hatsukade et al. 2013; Ono et al. 2014; Carniani et al. 2015) for the deep (A), medium-deep (B), and cluster (C) datasets. We multiply -1 to each pixel value of our ALMA maps, and perform the source extraction for negative peaks in the same manner as those in Section 3.1. The numbers of negative and positive peaks in our ALMA maps are shown in Figure 2. The excess of the positive to negative peak numbers is regarded as the real source numbers. We model the negative and positive peak distributions of Figure 2 with the functions of signal-to-noise ratio SNR,

$$N_{np}^c = a_n \times 10^{-b_n \times \text{SNR}}, \quad (1)$$

$$N_{pp}^c = a_n \times 10^{-b_n \times \text{SNR}} + a_p \times 10^{-b_p \times \text{SNR}}, \quad (2)$$

where N_{np}^c and N_{pp}^c are the cumulative numbers of negative and positive peaks, respectively, and a_n , b_n , a_p , and b_p are free parameters.

We estimate spurious source rates f_{sp} defined by the ratio of negative to positive peak numbers,

$$f_{sp}(\text{SNR}) = \frac{N_{np}^c(\text{SNR})}{N_{pp}^c(\text{SNR})}. \quad (3)$$

We evaluate f_{sp} with the best-fit functions of eqs. (1) and (2), and present f_{sp} in Figure 3.

Figures 3 indicates that the field data of deep (A) and medium-deep (B) have an almost identical distribution of the spurious source rates, while the cluster data (C) shows spurious source rates higher than (A) and (B) at a given SNR. This result would suggest that spurious source rates do not depend on the data depth, but the

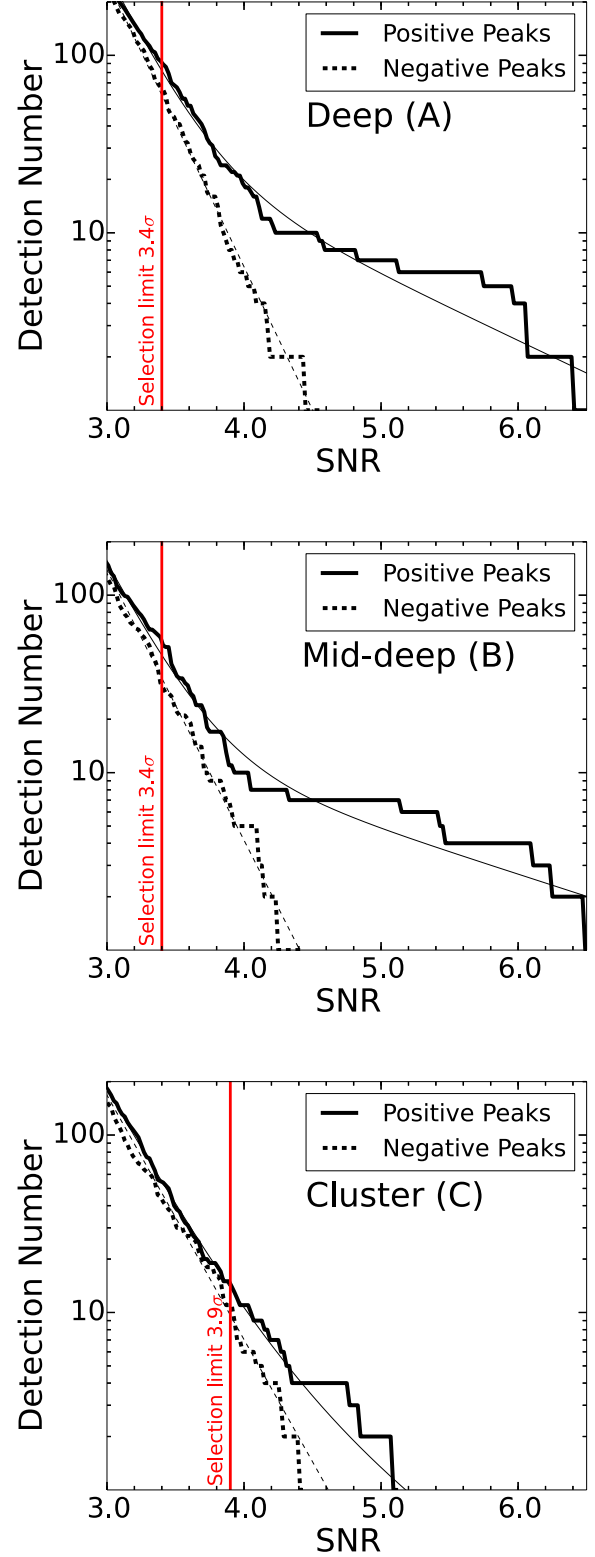


Figure 2. Total numbers of positive and negative peaks in the deep (A), medium-deep (B), and cluster (C) sub-datasets as a function of SNR. The thick solid and dashed lines show the total numbers of the positive and negative peaks, respectively. The thin solid and dashed curves denote the best-fit model functions. The red lines are selection limits for our source catalog. See text for more details.

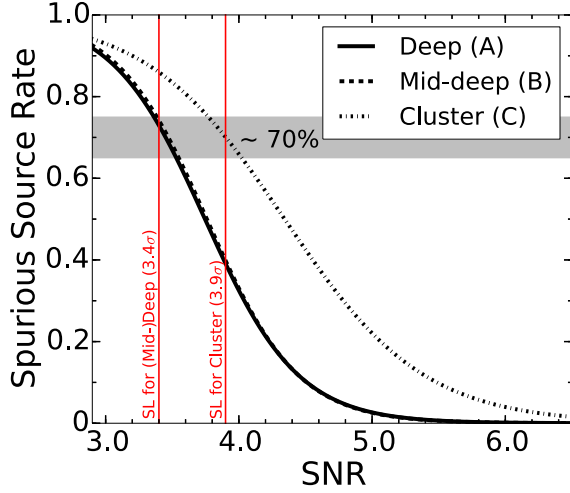


Figure 3. Cumulative spurious source rates as a function of SNR. The solid, dashed, and dotted lines indicate the deep (A), medium-deep (B), and cluster (C) sub-datasets, respectively. The red lines at SNRs of 3.4 and 3.9 are the selection limits (SL) of our source catalog.

mapping modes. The complex distribution of the depths in the mapping data of (C) would have the relation of SNR and spurious source rate that is different from the smooth distribution of the depth in the single pointing data of (A) and (B). We use sources down to an SNR whose spurious source rate is $\lesssim 70\%$, and adopt 3.4, 3.4, and 3.9 σ levels for our selection limits of the data (A), (B), and (C), respectively. Applying these selection limits to our 3.0 σ -detection catalog, we obtain a source catalog consisting of 133 sources: 122 from the field data (A and B) and 11 from the cluster data (C). The source catalog of our 133 faint ALMA sources is presented in Table 3.

Note that A1689-zD1, an LBG at $z = 7.5$ behind A1689 (Watson et al. 2015), is not included in our source catalog because A1689-zD1 is located outside of the primary beam with a $> 50\%$ sensitivity that is one of our selection criteria. Nevertheless, we have looked at the position of A1689-zD1 in our data, and found that there is a source with an SNR of 4 whose flux is the same as the one derived by Watson et al. (2015) within the $\sim 1\sigma$ uncertainty. We confirm the ALMA source detection at the position of A1689-zD1.

3.3. Completeness and Flux Boosting

We estimate the detection completeness by Monte-Carlo simulations. We put a flux-scaled synthesized beam into a map as an artificial source on a random position. These artificial sources have SNRs ranging from 3.0 to 7.0 with an SNR step of 0.2 dex. If an artificial source is extracted within a distance of the synthesized beam size from the input position, we regard that the source is recovered. These completeness estimations are conducted in the data before primary beam corrections, because we perform the source extractions in the real data (Section 3.1) uncorrected for primary beam attenuations. For all of our ALMA maps, we iterate this process 100 times at an SNR bin. Figure 4 displays our completeness

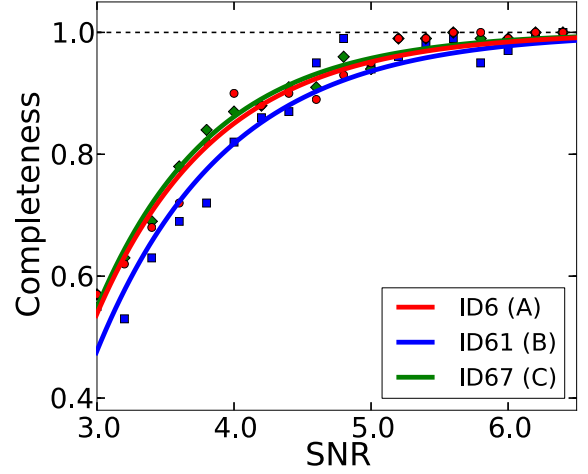


Figure 4. Completeness as functions of SNR for three sub-datasets. The circles (red line), squares (blue line), and diamonds (green line) represent the completeness values (the best-fit functions) of the ID 6, 61 and 67 maps, respectively.

estimates for three sub-datasets. We fit the function of $1 - \exp(a\text{SNR} - b)$ to our completeness estimates, where a and b are free parameters. The best-fit functions are also shown in Figure 4.

We examine the flux boosting that is caused by the confusions of the undetected faint sources (Austermann et al. 2009, 2010). We use the detected objects of the Monte-Carlo simulations conducted for the completeness estimates, and measure the output flux densities at the input positions. We find that the ratios of the input to output flux densities are almost unity with a variance of only 5% over the wide SNR range of our ALMA maps. This small flux boosting is probably found, because the angular resolution of ALMA is high. We thus conclude that the effect of flux boosting is negligibly small.

3.4. Flux Measurement

We estimate the source fluxes of our 133 objects from the integrated flux densities measured with the 2D Gaussian-fitting routine of *imfit* in CASA. Because the integrated flux density values for low-SNR sources would include large systematic uncertainties originated from the spatially-correlated positive noise at around the source position, we use the integrated flux densities of *imfit* only for the sources which are identified as 'resolved' with an SNR of ≥ 5 . For the rest of the sources, we use the peak fluxes of the *imfit* best-fit Gaussian measurements. We confirm that the peak flux values of *imfit*, S_{imfit} , agree with those of SExtractor, S_{SEx} , within the 1σ error, $S_{\text{imfit}}/S_{\text{SEx}} = 0.93 \pm 0.15$.

Because the sources in the cluster data of A1689 would be distorted by the gravitational lensing effects, we make a low-resolution map of A1689 produced with a $1''$ circular gaussian uv-taper that is the same as the one produced by Watson et al. (2015). The tapered beam size is $1''.31 \times 1''.12$. In this map, we perform the *imfit* flux measurements (as described above) at the source positions determined in the original map. Here we de-

fine flux measurements in the tapered and non-tapered maps as S_{taper} and $S_{\text{no taper}}$, respectively. We then obtain $S_{\text{taper}}/S_{\text{no taper}} = 1.01 \pm 0.19$ on average, if we omit two sources showing signatures of source confusions by neighboring objects. However, the strongly-lensed source of A1 shows a systematically high fraction of $S_{\text{taper}}/S_{\text{no taper}} = 1.23$. Thus, we decide to use S_{taper} for the cluster data of A1689, except for those two confusion sources. We also make low-resolution maps for some of the field data, and perform the same test of tapering. Because we find that S_{taper} and $S_{\text{no taper}}$ are almost identical in these data, we use $S_{\text{no taper}}$ for the field data.

We test the reliability of our flux measurements, performing flux recovery simulations. First, we select the typical data sets of ID22 and ID55 that have beam sizes of $\sim 0''.8$ and $\sim 1''.2$ corresponding to the two peaks of bimodal size distribution for our data. We then create 200 input sources of elliptical Gaussian model profiles with the uniform distribution of SNRs in 3 – 7 and major-axis sizes of $0''.2$ and $0''.5$. Here, the input source sizes are chosen from recent ALMA high-resolution studies. Ikarashi et al. (2014) and Simpson et al. (2015b) claim that the median sizes of individual submm sources are $\sim 0''.2 - 0''.3$ in FWHM. Simpson et al. (2015b) also find

that the stacked image of submm sources with a low SNR of 4 – 5 has the size of FWHM $0''.35^{+0.17}_{-0.10}$. Thus, we investigate the model sources of $0''.2$ and $0''.5$ that are taken from the median individual source size and the 1σ upper limit stacked source size. We add these model sources to ID22 and ID55 maps at random positions. Finally, we obtain flux densities of the model sources in the same manner as our flux measurements for the real sources, and compare these flux measurements with the input source fluxes. In the case of the $0''.2$ input source size, we find that the flux recovery ratio (defined by the ratio of the output to input fluxes) is 1.0 ± 0.1 (1.0 ± 0.2) for ID22 (ID55) data. Similarly, in the case of the $0''.5$ input source size, we obtain 0.8 ± 0.1 (0.9 ± 0.2) for ID22 (ID55) data. These results suggest that the flux recovery ratios are nearly unity within the $1 - 2\sigma$ uncertainties, and that our flux measurements are reliable.

Note that missing fluxes of interferometric observations are negligible. ALMA proposer's guide ⁵ shows that there exist missing flux effects for sources with $\simeq 2''.0 - 3''.0$ at Band 6/7 for the shortest-baseline configuration that we use. The source sizes of $\simeq 2''.0 - 3''.0$ are significantly larger than our ALMA sources whose angular sizes are $\lesssim 0''.5$, and the missing fluxes should be negligible.

Table 3
Source Catalog

ID	Map ID	R.A.(J2000)	Decl.(J2000)	$S_{\lambda_{\text{obs}}}^{\text{obs}}$ (mJy)	$S_{1.2\text{mm}}^{\text{corr}}$ (mJy)	SNR	f_{sp}
(1)	(2)			(3)	(4)	(5)	(6)
1	1	337.049805	-35.169643	0.06 ± 0.02	0.07 ± 0.02	3.6	0.57
2	1	337.050232	-35.164864	0.41 ± 0.01	0.68 ± 0.07	39.3	0.00
3	1	337.050293	-35.170044	0.07 ± 0.02	0.09 ± 0.02	4.0	0.34
4	1	337.053314	-35.165119	0.06 ± 0.01	0.12 ± 0.02	5.7	0.00
5	1	337.054413	-35.167576	0.05 ± 0.01	0.07 ± 0.02	4.1	0.27
6	1	337.054718	-35.166332	0.05 ± 0.01	0.06 ± 0.02	3.5	0.66
7	2	148.887314	18.150942	0.05 ± 0.01	0.04 ± 0.02	3.6	0.63
8	2	148.891403	18.151211	0.06 ± 0.02	0.06 ± 0.02	3.4	0.71
9	3	34.446007	-5.008159	0.05 ± 0.01	0.05 ± 0.02	3.5	0.70
10	3	34.446648	-5.007715	0.05 ± 0.01	0.04 ± 0.02	3.4	0.70
11 [†]	4	34.437332	-5.492185	0.06 ± 0.02	0.04 ± 0.01	3.7	0.53
12 [†]	4	34.437649	-5.494778	0.06 ± 0.02	0.03 ± 0.01	3.5	0.67
13 [†]	4	34.437805	-5.494339	0.06 ± 0.01	0.03 ± 0.01	3.8	0.48
14 [†]	4	34.439056	-5.494986	0.06 ± 0.02	0.03 ± 0.01	3.6	0.60
15 [†]	4	34.440075	-5.494945	0.07 ± 0.02	0.04 ± 0.01	3.6	0.63
16	5	121.593948	-41.376675	0.10 ± 0.03	0.08 ± 0.04	3.6	0.60
17	5	121.596870	-41.375671	0.06 ± 0.02	0.08 ± 0.02	3.6	0.63
18	5	121.599480	-41.373417	0.08 ± 0.02	0.10 ± 0.03	3.7	0.55
19	5	121.599564	-41.375568	0.07 ± 0.02	0.08 ± 0.03	3.6	0.61
20	5	121.600471	-41.375629	0.08 ± 0.02	0.09 ± 0.03	3.6	0.60
21	7	336.940674	-35.119549	0.11 ± 0.03	0.13 ± 0.04	3.8	0.48
22	8	201.001526	27.413574	0.10 ± 0.03	0.11 ± 0.04	3.5	0.70
23	8	201.001526	27.413574	0.10 ± 0.03	0.11 ± 0.04	3.5	0.70
24	8	201.001526	27.413574	0.10 ± 0.03	0.11 ± 0.04	3.5	0.70
25	9	325.760986	6.904217	0.13 ± 0.04	0.17 ± 0.05	3.5	0.68
26	9	325.762177	6.902022	0.14 ± 0.04	0.17 ± 0.05	3.6	0.62
27	9	325.763336	6.905892	0.08 ± 0.02	0.10 ± 0.03	3.4	0.72
28	9	325.767029	6.902850	0.15 ± 0.04	0.16 ± 0.05	3.6	0.60
29	10	352.281616	-3.033988	0.13 ± 0.04	0.12 ± 0.04	3.4	0.71
30	10	352.284851	-3.031080	0.16 ± 0.03	0.16 ± 0.03	5.9	0.00
31	10	352.285248	-3.030138	0.17 ± 0.04	0.17 ± 0.04	4.6	0.08
32	10	352.285309	-3.035150	0.11 ± 0.03	0.10 ± 0.03	3.8	0.47
33	11	200.929321	27.340736	0.15 ± 0.04	0.13 ± 0.04	3.9	0.40
34	12	150.547440	1.910628	0.13 ± 0.04	0.13 ± 0.05	3.7	0.55
35	13	351.831116	6.267834	0.13 ± 0.03	0.12 ± 0.03	4.2	0.22
36	13	351.833496	6.267574	0.16 ± 0.04	0.15 ± 0.04	3.7	0.53

⁵ Table A2 of the ALMA proposers' guide: <https://almascience.nao.ac.jp/documents-and-tools/cycle-1/alma->

Table 3 — *Continued*

ID	Map ID	R.A.(J2000)	Decl.(J2000)	$S_{\lambda_{\text{obs}}}^{\text{obs}}$ (mJy) (3)	$S_{1.2\text{mm}}^{\text{corr}}$ (mJy) (4)	SNR	f_{sp} (6)
(1)	(2)					(5)	
37	14	13.760888	1.771644	0.10 ± 0.03	0.08 ± 0.02	4.0	0.35
38	14	13.761566	1.768838	0.16 ± 0.04	0.12 ± 0.04	3.7	0.52
39	14	13.763390	1.770106	0.11 ± 0.03	0.08 ± 0.03	3.7	0.52
40	14	13.764014	1.770272	0.13 ± 0.03	0.09 ± 0.03	3.7	0.50
41	15	149.775772	1.736944	0.16 ± 0.03	0.18 ± 0.04	5.1	0.02
42	15	149.775955	1.738510	0.15 ± 0.04	0.17 ± 0.05	3.9	0.41
43	15	149.776794	1.736661	0.09 ± 0.03	0.07 ± 0.03	3.6	0.63
44	18	337.254547	14.950516	0.17 ± 0.05	0.14 ± 0.04	3.8	0.48
45	18	337.256073	14.954236	0.19 ± 0.03	0.21 ± 0.03	6.1	0.00
46	19	149.722565	2.606706	0.11 ± 0.03	0.10 ± 0.04	3.4	0.70
47	19	149.724045	2.602218	0.21 ± 0.05	0.28 ± 0.07	4.1	0.26
48	20	149.792572	2.103762	0.12 ± 0.03	0.10 ± 0.04	4.0	0.30
49	21	32.553406	-4.939113	0.12 ± 0.03	0.11 ± 0.03	3.9	0.37
50	21	32.553787	-4.939454	0.11 ± 0.03	0.15 ± 0.03	3.7	0.56
51	21	32.555397	-4.937203	0.13 ± 0.03	0.13 ± 0.04	3.7	0.54
52 [†]	22	150.127991	2.288839	0.13 ± 0.04	0.08 ± 0.03	3.4	0.72
53	23	359.017120	19.607481	0.10 ± 0.03	0.08 ± 0.03	3.4	0.71
54	24	150.406784	2.034714	0.14 ± 0.04	0.12 ± 0.04	3.5	0.64
55	25	150.393936	1.998264	0.15 ± 0.04	0.16 ± 0.05	3.7	0.56
56	26	34.100346	-5.154171	0.15 ± 0.04	0.14 ± 0.05	3.5	0.64
57	26	34.100658	-5.156616	0.16 ± 0.05	0.17 ± 0.06	3.5	0.66
58	26	34.102978	-5.155593	0.15 ± 0.04	0.15 ± 0.05	3.4	0.70
59	27	34.034069	-5.104988	0.17 ± 0.04	0.18 ± 0.06	3.8	0.45
60	28	34.472076	-4.711596	0.26 ± 0.07	0.27 ± 0.09	3.5	0.65
61	28	34.473747	-4.713997	0.16 ± 0.04	0.20 ± 0.06	3.6	0.62
62	29	34.392979	-5.043759	0.17 ± 0.04	0.19 ± 0.06	3.7	0.51
63	29	34.396526	-5.042582	0.21 ± 0.06	0.23 ± 0.07	3.6	0.59
64	29	34.396526	-5.046781	0.25 ± 0.07	0.26 ± 0.09	3.4	0.72
65	31	34.612003	-4.588018	0.25 ± 0.07	0.28 ± 0.08	3.5	0.69
66	31	34.612686	-4.583063	0.36 ± 0.07	0.43 ± 0.09	4.9	0.04
67	31	34.613739	-4.588505	0.31 ± 0.09	0.31 ± 0.10	3.5	0.68
68	31	34.613930	-4.585264	0.19 ± 0.06	0.18 ± 0.06	3.5	0.70
69	33	34.272991	-4.859830	0.29 ± 0.08	0.34 ± 0.11	3.5	0.68
70	33	34.274231	-4.860201	0.32 ± 0.09	0.43 ± 0.12	3.6	0.59
71	33	34.274761	-4.859237	0.26 ± 0.07	0.32 ± 0.09	3.8	0.46
72	34	34.305080	-5.067344	0.29 ± 0.07	0.39 ± 0.10	3.9	0.41
73	34	34.305538	-5.069685	0.23 ± 0.06	0.33 ± 0.09	3.6	0.61
74	34	34.305553	-5.067293	0.29 ± 0.07	0.22 ± 0.09	4.2	0.19
75	34	34.307556	-5.071889	0.33 ± 0.09	0.48 ± 0.12	3.6	0.61
76	34	34.309822	-5.069085	0.29 ± 0.08	0.23 ± 0.11	3.5	0.65
77 [†]	35	230.738800	-0.125928	0.35 ± 0.10	0.23 ± 0.07	3.5	0.69
78 [†]	35	230.739777	-0.125576	0.28 ± 0.08	0.20 ± 0.06	3.6	0.59
79 [†]	35	230.743118	-0.127994	0.28 ± 0.08	0.18 ± 0.06	3.5	0.66
80	36	34.327038	-5.131583	0.21 ± 0.06	0.27 ± 0.09	3.8	0.48
81	37	34.401154	-5.152167	0.33 ± 0.10	0.37 ± 0.15	3.4	0.72
82	37	34.401531	-5.154098	0.30 ± 0.08	0.34 ± 0.13	3.7	0.55
83	37	34.403275	-5.149917	0.36 ± 0.11	0.61 ± 0.18	3.4	0.71
84 [†]	38	231.036255	-0.176025	0.39 ± 0.11	0.22 ± 0.08	3.5	0.67
85 [†]	38	231.037949	-0.178142	0.22 ± 0.06	0.15 ± 0.04	3.7	0.54
86	40	34.414261	-5.201880	0.34 ± 0.10	0.56 ± 0.16	3.5	0.65
87	40	34.419544	-5.199385	0.31 ± 0.08	0.52 ± 0.14	3.8	0.46
88	41	149.590530	2.807018	0.28 ± 0.07	0.23 ± 0.05	4.2	0.21
89	41	149.591949	2.805352	0.26 ± 0.07	0.21 ± 0.05	4.0	0.31
90	42	150.688171	2.681118	0.37 ± 0.07	0.26 ± 0.06	5.4	0.01
91	45	34.194702	-5.056259	0.43 ± 0.12	0.39 ± 0.15	3.5	0.71
92	45	34.197121	-5.059778	0.31 ± 0.08	0.37 ± 0.10	3.7	0.55
93	46	150.409714	2.358208	0.30 ± 0.09	0.32 ± 0.09	3.5	0.71
94	47	149.770050	1.804996	0.32 ± 0.09	0.31 ± 0.10	3.4	0.72
95	48	34.411190	-4.745051	0.30 ± 0.08	0.14 ± 0.09	3.8	0.44
96	48	34.411701	-4.745893	0.31 ± 0.08	0.34 ± 0.09	4.0	0.31
97	49	150.600494	2.444365	0.47 ± 0.13	0.53 ± 0.14	3.6	0.59
98	51	34.440269	-4.912953	0.39 ± 0.11	0.40 ± 0.12	3.6	0.60
99	51	34.441357	-4.912045	0.32 ± 0.08	0.29 ± 0.09	3.9	0.43
100	51	34.441635	-4.913539	0.46 ± 0.13	0.45 ± 0.14	3.6	0.62
101	51	34.442795	-4.911066	0.53 ± 0.08	0.56 ± 0.11	6.2	0.00
102	51	34.443920	-4.909602	0.41 ± 0.12	0.35 ± 0.13	3.5	0.65
103	52	150.151459	1.751314	0.49 ± 0.14	0.50 ± 0.13	3.6	0.64
104	54	34.759140	-4.832398	0.32 ± 0.09	0.37 ± 0.11	3.5	0.71
105	55	150.022736	2.027032	0.53 ± 0.08	0.46 ± 0.08	6.8	0.00
106	57	34.141144	-5.232085	0.47 ± 0.13	0.42 ± 0.15	3.6	0.60
107	58	34.303791	-5.161064	0.47 ± 0.14	0.58 ± 0.16	3.4	0.73
108	59	150.201645	2.021740	0.57 ± 0.15	0.72 ± 0.22	3.7	0.53
109	60	34.250214	-4.804325	0.34 ± 0.09	0.34 ± 0.10	3.9	0.39

Table 3 — *Continued*

ID	Map ID	R.A.(J2000)	Decl.(J2000)	$S_{\lambda_{\text{obs}}}^{\text{obs}}$ (mJy) (3)	$S_{1.2\text{mm}}^{\text{corr}}$ (mJy) (4)	SNR	f_{sp}
(1)	(2)					(5)	(6)
110	60	34.250927	-4.802006	0.37 ± 0.11	0.39 ± 0.13	3.5	0.68
111	61	34.744495	-4.855921	0.35 ± 0.10	0.27 ± 0.12	3.5	0.70
112	61	34.747295	-4.858103	0.37 ± 0.10	0.26 ± 0.11	3.8	0.45
113	62	150.757401	1.700786	0.50 ± 0.14	0.57 ± 0.21	3.5	0.70
114	62	150.758331	1.703298	0.42 ± 0.12	0.52 ± 0.17	3.6	0.60
115	62	150.760971	1.703856	1.01 ± 0.10	1.17 ± 0.18	9.7	0.00
116	62	150.762024	1.698676	0.57 ± 0.16	0.85 ± 0.24	3.5	0.69
117	62	150.762161	1.701653	0.34 ± 0.10	0.37 ± 0.14	3.5	0.68
118	62	150.762741	1.700690	0.43 ± 0.12	0.61 ± 0.17	3.6	0.62
119	62	150.763138	1.702965	0.47 ± 0.13	0.70 ± 0.19	3.6	0.62
120	64	34.587593	-5.318766	0.32 ± 0.09	0.21 ± 0.10	3.6	0.59
121	64	34.589180	-5.315989	0.61 ± 0.17	0.69 ± 0.21	3.5	0.65
122	65	34.387825	-5.220457	0.41 ± 0.11	0.42 ± 0.13	3.7	0.51
123	67	197.860764	-1.337225	0.25 ± 0.06	$0.03^{\ddagger} \pm 0.01$	4.3	0.53
124	67	197.862061	-1.342226	0.24 ± 0.06	$0.00^{\ddagger} \pm 0.00$	4.3	0.54
125	67	197.864731	-1.343368	0.27 ± 0.06	$0.03^{\ddagger} \pm 0.01$	4.7	0.32
126	67	197.869086	-1.337143	0.31 ± 0.08	$0.08^{\ddagger} \pm 0.03$	4.1	0.60
127	67	197.871590	-1.345783	0.30 ± 0.06	$0.02^{\ddagger} \pm 0.01$	5.1	0.20
128	67	197.874725	-1.326138	0.22 ± 0.05	$0.02^{\ddagger} \pm 0.01$	4.3	0.51
129	67	197.881638	-1.323127	0.26 ± 0.05	$0.05^{\ddagger} \pm 0.02$	4.8	0.29
130	67	197.882812	-1.356609	0.28 ± 0.07	$0.05^{\ddagger} \pm 0.02$	4.1	0.64
131	67	197.883881	-1.355241	0.30 ± 0.08	$0.06^{\ddagger} \pm 0.03$	4.0	0.65
132	67	197.884125	-1.334885	0.30 ± 0.07	$0.13^{\ddagger} \pm 0.05$	4.2	0.58
133	67	197.886185	-1.328756	0.24 ± 0.05	$0.04^{\ddagger} \pm 0.01$	5.1	0.19

Note. — (1): Source ID. (2): Map ID that corresponds to the one in Table 2. (3): Peak flux density of the SExtractor measurement (Section 3.1) with the primary beam correction at the observed wavelength. (4): The best-estimate source flux density at 1.2 mm. The source flux is estimated with the 2D Gaussian-fitting routine of *imfit* in CASA (Section 3.4) with the primary beam correction and the flux scaling to 1.2 mm (Section 3). For the sources found in the cluster data, the lensing magnification corrections are also applied (Section 3.5). The lensing magnification factors are estimated at the ALMA flux peak positions. The error bar includes the random noise, 10% of ALMA system’s flux measurement uncertainty, and the lensing magnification uncertainty (Section 4.1). (5): Signal-to-noise ratio of the peak flux density. (6): Spurious source rate that is defined by eq. 3. [†] Source identified in the Band 7 map. Unless otherwise specified, the source is found in the Band 6 map. [‡] The lensing magnification is corrected. The ID 124 source has 0.0020 ± 0.0010 mJy for the best-estimate source flux density at 1.2 mm with the primary-beam and lensing-magnification corrections.

3.5. Mass Model

We construct a mass model for the cluster data (C) of A1689 at $z = 0.183$. We make the mass model with the parametric gravitational lensing package GLAFIC (Oguri 2010) in the same manner as Ishigaki et al. (2015). Our mass model consists of three types of mass distributions: cluster-scale halos, cluster member galaxy halos, and external perturbation. For evaluating the mass distributions, we make a galaxy catalog of A1689, conducting source extractions in the optical images of g_{475} , r_{625} , and i_{775} bands taken with *Hubble Space Telescope* (HST). The cluster-scale halos are estimated with three brightest member galaxies in the core of the cluster. The cluster member galaxies are selected by the color criteria of

$$r_{625} < 24,$$

$$g_{475} - r_{625} < -\frac{1}{18}(r_{625} - 24) + 1.3,$$

$$g_{475} - r_{625} > -\frac{1}{18}(r_{625} - 24) + 0.7, \quad (4)$$

where the source extraction and photometry are carried out with SExtractor. The external perturbation is calculated with the theoretical model under the assumption that the perturbation is weak (e.g., Kochanek 1991).

Using the positions of the multiple images presented in the literature (Coe et al. 2010; Diego et al. 2015), we optimize free parameters of the mass profiles based on the standard χ^2 minimization to determine the best-fit mass model. Figure 1 presents the best-fit mass model. The best-fit mass model achieves that all of the offsets between the model and observed positions of multiple images are within $1''0$ in the image plane. We then calculate magnification factors μ at the positions of our sources. For the μ estimates, we assume our source redshift of $z = 2.5$ that is the same as the one used in the flux scaling shown in Section 3. This assumption does not change our statistical results, because most of mm sources in the target fields at the high-galactic latitude should reside at $z > 1$ where the μ values do not depend much on a redshift. Here we calculate the magnification factors for sources at $z = 7.5$ that correspond to the redshift of A1689-zD1, and evaluate the differences between the magnification factors for sources at $z = 2.5$ ($\mu_{2.5}$) and $z = 7.5$ ($\mu_{7.5}$). We find that the average difference, $\Delta\mu \equiv (\mu_{7.5} - \mu_{2.5})/\mu_{2.5}$, is 0.36 ± 0.25 for our 11 sources in A1689. Although the difference is not large, we include the lensing magnification difference of 0.36 into the errors of the intrinsic flux estimates for our 11 sources in A1689. Accordingly, we propagate these uncertainties to our major results such as number counts shown in Section 4.

3.6. Survey Area

We estimate survey areas of our data of A, B, and C, and present these estimates in Figure 5. The survey

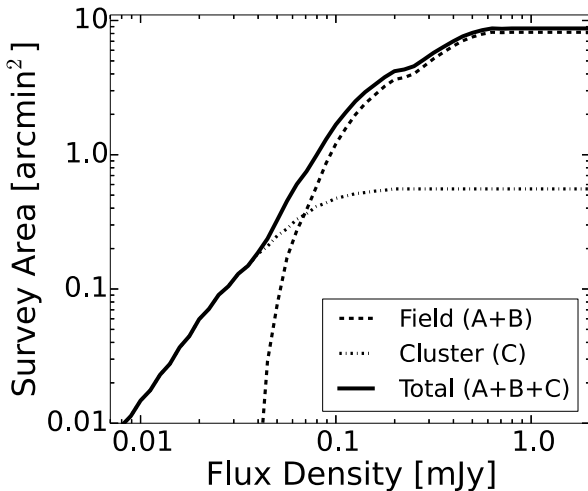


Figure 5. Survey areas as a function of intrinsic flux densities. The dashed, dotted, and solid lines represent the survey areas of the field (A and B), cluster (C), and total (A, B, and C) datasets, respectively.

areas are defined by the high sensitivity regions that are detailed in Section 3.1. Because the sensitivities of our ALMA maps are not spatially uniform, the survey areas depend on the flux densities.

In the field data of A and B, the sensitivity of the primary beam decreases with increasing radius from a map center. In other words, the detectable intrinsic flux densities (corrected for the primary beam attenuation) increase from the center to the edge of the data. First, we find the radius where sources with the intrinsic flux densities can be detected at our selection limit SNR. Then, we calculate areas with the radius given in each map, and sum up these areas to obtain the total survey areas.

In the cluster data of C, the spatial distribution of the sensitivity is not expressed by a simple function of radius, because the cluster data are taken by mosaic mapping. Moreover, there are cluster-lensing magnification effects that allow us to detect intrinsically faint sources. We make an effective magnification map, multiplying, at each position, the sensitivity and the magnification factor estimated with the mass model of Section 3.5. We then calculate the survey area of the C data where a source with an intrinsic flux density can be observed above the selection limit.

4. NUMBER COUNTS AND EBL

4.1. Number Counts at 1.2 mm

We derive differential number counts at 1.2 mm. For the number counts, we use the 122 sources identified in the ALMA Band 6 maps covering the 1.2 mm band, because there is a possibility that the 11 sources in the Band 7 would include unknown systematics in the flux scaling to 1.2 mm fluxes (Section 3). To derive the number counts, we basically follow the methods used in the previous ALMA studies (Hatsukade et al. 2013; Ono et al. 2014; Carniani et al. 2015). A contribution from an identified source with an intrinsic flux density of S to the

number counts, ξ , is determined by

$$\xi(S) = \frac{1 - f_{\text{sp}}(S)}{C(S)A_{\text{eff}}(S)}, \quad (5)$$

where C is the completeness, and A_{eff} is the survey area. For C , A_{eff} , and f_{sp} (eq.3), we use the values derived in Section 3. Then, we calculate a sum of the contributions for each flux bin,

$$n(S) = \frac{\sum \xi(S)}{\Delta \log S}, \quad (6)$$

where $\Delta \log S$ is the scaling factor of 0.25 for the 1-dex width logarithmic differential number counts. We estimate the errors that include both Poisson statistical errors of the source numbers and flux uncertainties of the identified sources. Because the numbers of our sources are small, we use the Poisson uncertainty values presented in Gehrels (1986) that are applicable for the small number statistics. The flux uncertainties are composed of the random noise and the ALMA system's flux measurement uncertainty whose typical value is $\sim 10\%$ (Section 2.3). Moreover, for our 11 sources in the A1689 data, the intrinsic flux estimates include the lensing magnification uncertainties (see Section 3.5). To evaluate these flux uncertainties, we perform Monte-Carlo simulations. We make a mock catalog of the faint ALMA sources whose flux densities follow the Gaussian probability distributions whose standard deviations are given by the combination of the random noise and the system (+ the lensing magnification) uncertainties. We obtain the number counts for each mock catalog in the same manner as those for our real sources. We repeat this processes 1000 times, and calculate the standard deviation of the number counts per flux bin caused by the flux uncertainties. Combining the standard deviation of the flux uncertainties with the Poisson errors, we finally obtain the 1σ uncertainties of the number counts.

The differential number counts and the associated 1σ uncertainties are shown in Figure 6 and Table 4. With the technique same as those deriving the differential number counts, we estimate the cumulative number counts that are summarized in Table 4.

In Figure 6, we find that the faintest data point at ~ 0.002 mJy (red open circle) is composed of a source with a very high magnification factor of $\mu > 100$. The highly magnified sources would potentially include large systematic uncertainties originated from the mass modeling. Moreover, the faintest data point has the large error bar that does not provide important constraints on the number count measurements. Thus, we do not use the faintest data point in the following discussion. Except for this very high magnification factor object, the faintest and brightest sources in our sample have intrinsic fluxes of 0.018 and 1.2 mJy, respectively. Thus, our study covers the flux density range of $\sim 0.02 - 1$ mJy.

4.2. Comparison with Previous Number Count Measurements

We compare our number counts to previous measurements at the ~ 1.2 mm band. In the flux range close to our study, there are two types of previous studies, blank-field observations with ALMA and cluster observations for lensed sources with single-dish telescopes. For the

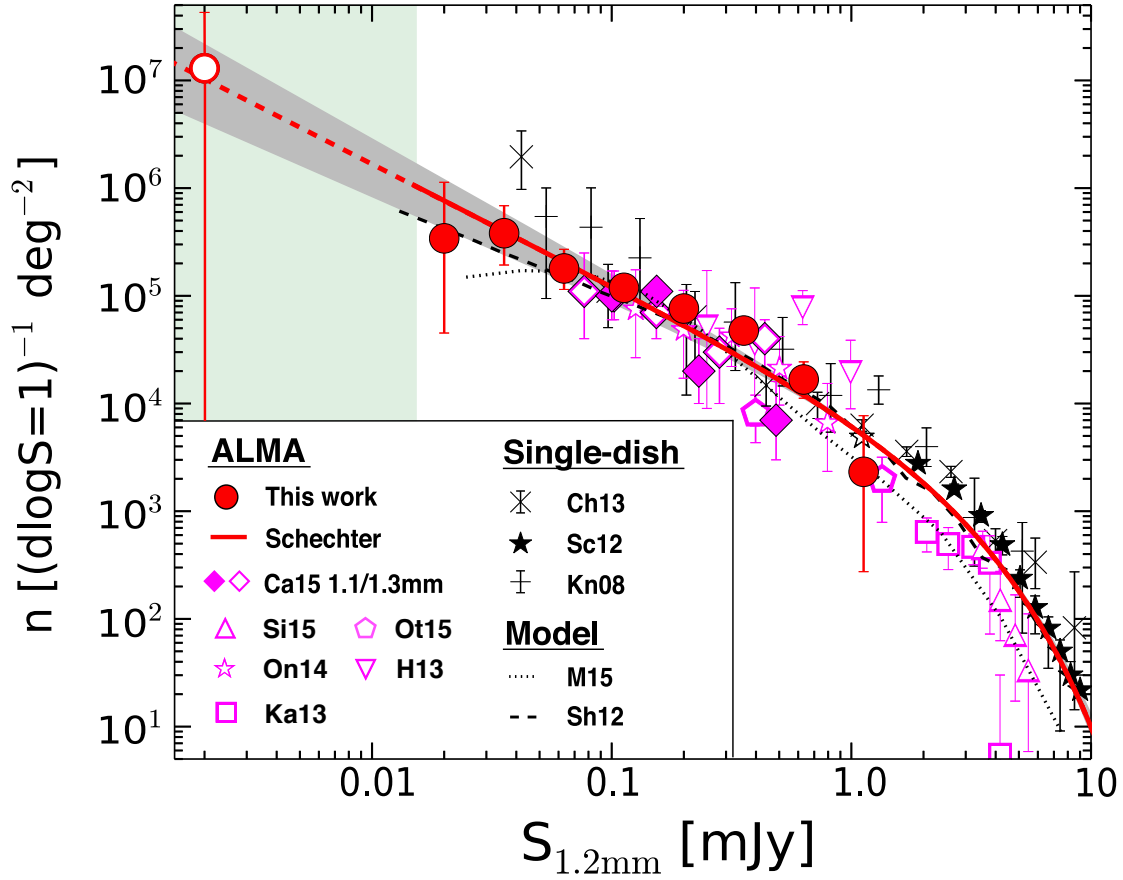


Figure 6. Differential number counts at 1.2 mm. The red filled circles are our number counts derived from our faint ALMA sources. The red curve and the gray region denote the best-fit Schechter function and the associated 1σ error. In the Schechter function fitting, we use our number counts and the previous measurements shown with the black filled stars (Sc12; Scott et al. 2012) and the magenta filled diamonds (Ca15 1.1 mm; Carniani et al. 2015). Note that the 1.1 mm results of Ca15 are obtained from ALMA sources, none of which are used in our number count measurements. Because the rest of the existing ALMA studies include some ALMA data covered by our study, for our Schechter function fitting we do not include the previous ALMA measurements shown with the magenta open squares (Ka13; Karim et al. 2013), open inverse triangles (H13; Hatsukade et al. 2013), open stars (O14; Ono et al. 2014), open diamonds (Ca15 1.3 mm; Carniani et al. 2015), open triangles (Si15; Simpson et al. 2015a), and open pentagons (Ot15; Oteo et al. 2015). Note that the faintest data point of our study (red open circle) is also removed from the sample of our Schechter function fitting, due to the possible large systematic uncertainties. The pale-green region presents a flux range where no reliable number-count data bin exists (see text). We do not use the faintest data point of Sc12 (black open star) for our fitting, because this data point has unrealistically small errors. The dashed and dotted curves show the model predictions for number counts based on cosmological hydrodynamic simulations with GADGET-3 (Sh12; Shimizu et al. 2012) and semi-analytic models (M15; Makiya et al. 2015), respectively. These model predictions are roughly consistent with our results. For the previous measurements of the number counts at 1.1 mm and 1.3 mm different from our 1.2 mm band, we scale the flux densities with the methods shown in Section 3. Since the flux scaling factors for < 1 mm wavelengths would contain relatively large systematic uncertainties, we do not use the < 1 mm band data, for our Schechter function fitting, that are presented with the open triangles (Kn08; Knudsen et al. 2008) and open hexagons (Ch13; Chen et al. 2013).

measurements of 1.1 and 1.3 mm bands that are different from 1.2 mm band, we scale the flux densities with the methods described in Section 3.

4.2.1. Blank-Field Observations

To derive number counts, Hatsukade et al. (2013) and Ono et al. (2014) use 20 ALMA maps in one blank field of SXDS and 10 ALMA maps in 10 independent fields, respectively. Carniani et al. (2015) obtain number counts with the 18 ALMA maps composed of 9 independent fields at 1.1 mm band and the 9 ALMA maps in one blank field of Cosmic Evolution Survey (COSMOS; Scoville et al. 2007) at 1.2 mm band. After the flux den-

sity scaling, all of these previous number counts agree with our measurements within the 1σ uncertainties. Because the amount of our ALMA data is much larger than the previous studies, the statistical and systematic uncertainties of the number counts measurements are significantly smaller than those of previous studies.

4.2.2. Cluster Observations for Lensed Sources

Single-dish observations of SCUBA and SCUBA-2 for lensed sources behind galaxy clusters successfully reach the intrinsic flux limits comparable to the previous ALMA blank field observations. Knudsen et al. (2008) conduct SCUBA observations for 12 clusters, and de-

Table 4
Differential and Cumulative Number
Counts at 1.2 mm

S (mJy)	$\log(n)$ $([\Delta \log S = 1]^{-1} \text{deg}^{-2})$	N_{diff}
(0.002)	$7.1^{+0.5}_{-7.1}$	1
0.020	$5.5^{+0.3}_{-0.5}$	2
0.036	$5.6^{+0.3}_{-0.4}$	6
0.063	$5.3^{+0.2}_{-0.4}$	15
0.112	$5.1^{+0.2}_{-0.2}$	25
0.200	$4.9^{+0.1}_{-0.2}$	27
0.356	$4.7^{+0.1}_{-0.2}$	29
0.633	$4.2^{+0.2}_{-0.5}$	15
1.124	$3.4^{+0.5}_{-1.3}$	2
S (mJy)	$\log(n(> S))$ (deg^{-2})	N_{cum}
(0.002)	$6.6^{+0.5}_{-1.1}$	122
0.015	$5.5^{+0.3}_{-0.4}$	121
0.027	$5.3^{+0.2}_{-0.3}$	119
0.047	$5.0^{+0.2}_{-0.2}$	113
0.084	$4.8^{+0.1}_{-0.2}$	98
0.150	$4.6^{+0.1}_{-0.1}$	73
0.267	$4.2^{+0.2}_{-0.2}$	46
0.474	$3.7^{+0.2}_{-0.3}$	17
0.843	$2.8^{+0.6}_{-0.5}$	2

Note. — The 1σ uncertainties are estimated from the combination of the number-count Poisson statistical errors and the flux uncertainties (see text). The column of N_{diff} presents the numbers of our 1.2 mm sources in each flux bin, while the one of N_{cum} denotes the cumulative source numbers down to the flux densities. For our analysis, we do not use the faintest bin data indicated with the parentheses (see text).

rive the number counts at $850 \mu\text{m}$ with the sample of 15 gravitationally lensed faint sources with flux densities below the SCUBA’s blank-field confusion limit (~ 2 mJy at $850 \mu\text{m}$). Chen et al. (2013) observe 2 clusters as well as 3 blank fields with SCUBA-2, and obtain the number counts similar to those of Knudsen et al. (2008). The number counts from these previous studies are also shown in Figure 6. These previous results generally agree with our results within the 1σ errors. Although the number counts of the previous studies are slightly higher than ours systematically at $\lesssim 0.1$ mJy, these small systematic differences would be explained by the uncertainties of the flux scaling from $850 \mu\text{m}$ to 1.2 mm.

4.3. Contributions to the EBL

In Section 4.1, we obtain the 1.2-mm number counts with our faint ALMA source. Because our sample lacks sources brighter than 1.2 mJy, we use previous studies of bright sources in the literature to investigate the source contributions to the IR EBL. There are a number of studies that investigate the bright sources (Figure 6), but we use the number counts at 2–10 mJy obtained from a survey for six blank fields with a single-dish telescope instrument of AzTEC (Scott et al. 2012), which shows reliable number counts at 1.1 mm that is close to 1.2 mm band. Although there is another systematic survey for bright sources from the single-dish observations with LABOCA (Weiß et al. 2009), we do not use their data for our anal-

ysis, due to their observation wavelength of $870 \mu\text{m}$ far from our 1.2 mm band. It should be noted that the number counts of bright sources are still under debate (e.g., Karim et al. 2013; Chen et al. 2013; Simpson et al. 2015a), because the recent high-resolution ALMA observations reveal multiple sources in a beam of single-dish observations (Hodge et al. 2013). Nevertheless, our results below do not depend on the bright-source number counts, because the contribution from the bright sources is not large (Section 1).

The source contributions to the IR EBL can be calculated by integrating the number counts down to a flux density limit. To characterize the shape of the number counts, we use the Schechter function form (Schechter 1976) in the same manner as the previous studies,

$$\phi(S)dS = \phi_* \left(\frac{S}{S_*} \right)^\alpha \exp \left(-\frac{S}{S_*} \right) d \left(\frac{S}{S_*} \right), \quad (7)$$

where ϕ_* , S_* , and α are the normalization, characteristic flux density, and faint-end slope power-law index, respectively. The logarithmic form of $n(S)d(\log S) = \phi(S)dS$ is given by

$$n(S) = (\ln 10) \phi_* \left(\frac{S}{S_*} \right)^{(\alpha+1)} \exp \left(-\frac{S}{S_*} \right). \quad (8)$$

Using eq. (8), we conduct χ^2 -fitting to the differential number counts derived from our and the previous observations shown with the filled symbols in Figure 6 that are our measurements and the AzTEC (Scott et al. 2012) and ALMA 1.1 mm (Carniani et al. 2015) results. Here we do not use the measurements of Hatsukade et al. (2013), Ono et al. (2014), Oteo et al. (2015), and the 1.3 mm results of Carniani et al. (2015) that are presented with the open symbols of Figure 6, because these studies use ALMA data covered by our study or the sample that does not meet our selection criteria (Section 2.2). We confirm that the entire ALMA 1.1 mm data of Carniani et al. (2015) are different from ours. Including the bright number counts at 2–10 mJy (see above), we perform Schechter function fitting with our number counts and those from the 1.1-mm observations with AzTEC (Scott et al. 2012) and ALMA (Carniani et al. 2015). We vary three Schechter parameters, and search for the best-fit parameter set of (ϕ_*, S_*, α) that minimizes χ^2 . The best-fit function and parameter set are presented in Figure 6 and Table 5, respectively. Figure 6 and the χ^2/dof of 16.9/19 (Table 5) indicate that the number counts are well represented by the Schechter function down to ~ 0.02 mJy.

We also carry out fitting of the double-power law (DPL) function in the same manner as the Schechter function fitting. The DPL function has four free parameters of ϕ_*^{DPL} , S_*^{DPL} , α^{DPL} , and β^{DPL} (see, e.g., Ono et al. 2014). The best-fit parameters are presented in Table 5. The χ^2/dof value for the DPL fitting is nearly unity (12.8/18), and the DPL also well represents the number counts. Because the Schechter and DPL functions show similarly good fitting results, we use the Schechter function fitting results for simplicity in the following discussion.

With the best-fit Schechter parameter set, we calculate the integrated flux densities, $\int_{S_{\text{limit}}}^{\infty} S \phi(S) dS$, down to the

Table 5
Best-fit Parameters

Schechter				
S_* (mJy) (1)	ϕ_* (10^3 deg^{-2}) (2)	α (3)	χ^2/dof (4)	
$2.35^{+0.16}_{-0.16}$	$1.54^{+0.29}_{-0.26}$	$-2.12^{+0.07}_{-0.06}$	16.6/19	
DPL				
S_*^{DPL} (mJy) (5)	ϕ_*^{DPL} (10^3 deg^{-2}) (6)	α^{DPL} (7)	β^{DPL} (8)	χ^2/dof
$4.43^{+0.34}_{-0.49}$	$0.26^{+0.05}_{-0.07}$	$2.39^{+0.05}_{-0.06}$	$6.20^{+0.48}_{-1.11}$	12.8/18

Note. — (1)-(3): Best-fit parameter set for the Schechter function. (4): χ^2 over the degree of freedom. (5)-(8): Best-fit parameter set for the DPL function.

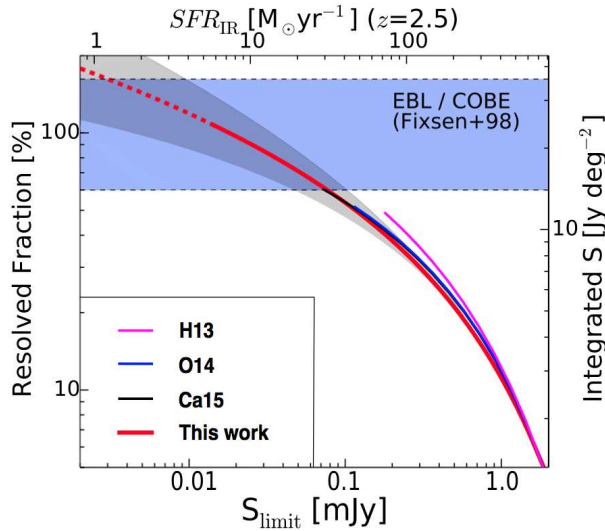


Figure 7. Fraction of resolved EBL at 1.2 mm as a function of the detection limit, S_{limit} . The red line and the gray shade indicate the best estimate from our study and the associated errors, respectively. The magenta, blue, and black lines present the estimates from the previous ALMA studies (Hatsukade et al. 2013; Ono et al. 2014; Carniani et al. 2015). Here we re-calculate the resolved fractions of the previous studies with the bright source counts of Scott et al. (2012). The blue shade denotes the IR EBL measurements from COBE (Fixsen et al. 1998). The right axis represents the absolute values of the integrated flux densities, $\int_{S_{\text{limit}}}^{\infty} S \phi(S) dS$, that correspond to the resolved EBL fraction. The top axis ticks IR star-formation rates SFR_{IR} corresponding to the 1.2 mm flux (Kennicutt 1998) for the case that a source resides at $z = 2.5$.

flux limit of S_{limit} . Because the faintest bin of our number count data covers down to 0.015 mJy (Figure 6), we choose $S_{\text{limit}} = 0.015$ mJy. We calculate the integrated flux density to be $22.9^{+6.7}_{-5.6}$ Jy deg^{-2} at 1.2 mm. Figure 7 shows the integrated flux density. We evaluate the fraction contributed to the total IR EBL measurement at 1.2 mm (22^{+14}_{-8} Jy deg^{-2} ; Fixsen et al. 1998) that is obtained by the observations of the COBE Far Infrared Absolute Spectrophotometer (FIRAS), and find that the resolved fraction in our study is $104^{+31}_{-25}\%$. This result suggests that our study fully resolves the 1.2 mm EBL into the individual sources within the uncertainties.

Our result also indicates that the EBL contribution of sources with $\lesssim 0.02$ mJy are negligibly small. It would

suggest that there is 1) a flattening of number counts slope α , or 2) a truncation of the number counts at a flux S_{trunc} below $\simeq 0.02$ mJy. Using our resolved fraction of $f_{\text{res}} = 104^{+31}_{-25}\%$, we constrain α and S_{trunc} in the scenarios of 1) and 2). For the scenario of 1), we extrapolate the Schechter function from S_{limit} to 0 mJy with a power law of $n(S) \propto S^{(\alpha_0 - S_{\text{limit}}) + 1}$, where $\alpha_0 - S_{\text{limit}}$ is a power law slope at 0 mJy to S_{limit} , and integrate the Schechter function with the power law extrapolation. We constrain the $\alpha_0 - S_{\text{limit}}$ value for the condition that the integrated flux density does not exceed the 1σ upper limit of the EBL measurement. We thus determine that the lower limit of $\alpha_0 - S_{\text{limit}} \gtrsim -1.0$. For the scenario of 2), we extrapolate our best-fit Schechter function below S_{limit} . We find $S_{\text{trunc}} \simeq 0.004$ mJy (corresponding to $SFR_{\text{IR}} \sim 1.6 M_{\odot} \text{yr}^{-1}$; Kennicutt 1998) where the 1σ lower error of f_{res} reaches 100% of the EBL contribution fraction. Because these 1) and 2) scenarios are two extreme cases, our results would suggest that the faint-end slope at $\lesssim 0.02$ mJy is flatter than the best-fit Schechter function slope of $\alpha = -2.12^{+0.07}_{-0.06}$ (Table 5), and that there is a number-counts truncation, if any, at $\lesssim 0.02$ mJy.

5. CLUSTERING ANALYSIS

5.1. Galaxy Bias of our Faint ALMA Sources

We estimate a galaxy bias of our faint ALMA sources by the counts-in-cells technique (e.g. Adelberger et al. 1998; Robertson 2010)

$$b_g^2 \approx \frac{\sigma_N^2 - \bar{N}}{\bar{N}^2 \sigma_V^2(z)}, \quad (9)$$

where σ_N^2 is the standard deviation of the detected source counts per field, σ_V^2 is the matter variance averaged over the survey volumes V , and \bar{N} is the average source counts per field.

In this counts-in-cells analysis, we use 66 maps of the field data (A) and (B). Because the cluster data (C) includes lensing effects of magnification and survey volume distortion as well as the different spurious source rate (Section 3.2), we do not include the cluster data (C) in the sample of our counts-in-cells analysis. The survey volume is calculated by using the average effective area per field (Section 3.6). For the redshift distribution to calculate the volume, we again assume a median redshift of $z = 2.5$ (Section 3) and the top hat function covering $z = 1 - 4$. For σ_N^2 and \bar{N} , we do not use the simple detection numbers, but the corrected detection numbers obtained with equation (5), which allows us to remove the effects of spurious sources. We calculate σ_V^2 with the analytic structure formation model (e.g., Mo & White 2002). To estimate the 1σ uncertainty of b_g , we carry out Monte-Carlo simulations. We first make 1000 mock catalogs of faint ALMA sources consisting of source counts that follow the Poisson probability distribution function whose average values agree with our observed source counts. Then, we calculate galaxy bias values with each mock catalog, and repeat this process for the 1000 mock catalogs. We define a 1σ error of our observational b_g estimate by the 68 percentile of the b_g distribution obtained from the 1000 mock catalog results. Because the 1σ error is large, we cannot obtain the measurement of b_g but place a 1σ upper limit of $b_g < 3.5$

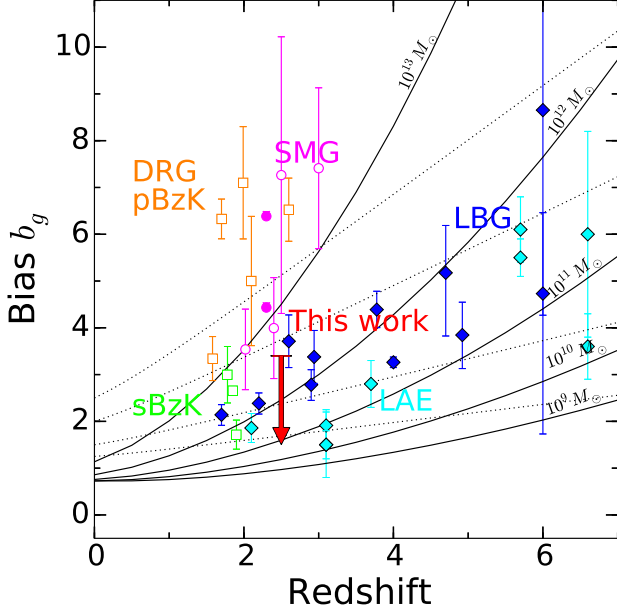


Figure 8. Galaxy bias of our faint ALMA sources and the other high- z galaxies. The red arrow shows the 1σ upper limit of our faint ALMA sources. The magenta arrows are the measurements and the upper limit for bright SMGs, which are calculated from the clustering results of Webb et al. (2003); Blain et al. (2004); Weiß et al. (2009); Williams et al. (2011); Hickox et al. (2012). The orange and green squares denote the K -selected galaxies of DRGs/pBzK and sBzK, respectively (Grazian et al. 2006; Hayashi et al. 2007; Quadri et al. 2007; Blanc et al. 2008; Furusawa et al. 2011; Lin et al. 2012). The blue and cyan diamonds represent the UV-selected galaxies of LBGs (including BX/BM) and LAEs, respectively (Ouchi et al. 2004; Adelberger et al. 2005; Overzier et al. 2006; Lee et al. 2006; Gawiser et al. 2007; Ouchi et al. 2010). The solid curves indicate the galaxy biases of the dark halos with masses of 10^9 , 10^{10} , 10^{11} , 10^{12} , and $10^{13} M_\odot$ from bottom to top, which are predicted by the model of Sheth & Tormen (1999) under the assumption of the one-to-one relation between galaxies and dark halos. The dotted curves present evolutionary tracks of dark halos for the galaxy conserving case, which assume that the motion of galaxy is purely caused by gravity with no galaxy merges (Fry 1996).

for our faint ALMA sources. This 1σ upper limit agrees with the previous b_g estimate for faint ALMA sources, $b_g < 4$, given by Ono et al. (2014).

We estimate the dark halo masses of our faint ALMA sources with our result of $b_g < 3.5$ with the analytics structure formation model of Sheth & Tormen (1999), assuming the one-to-one correspondence between galaxies and dark halos. We obtain the 1σ upper limit dark halo mass of $\lesssim 5 \times 10^{12} M_\odot$.

5.2. Comparison with Other Populations

Figure 8 shows the galaxy biases of our faint ALMA sources and a variety of high- z galaxy populations; bright SMGs, K -selected galaxies including passively evolving BzK galaxies (pBzKs) and star-forming BzK galaxies (sBzKs), distant red galaxies (DRGs), and UV-selected galaxies composed of BX/BM galaxies, LBGs, and LAEs. Some of these high- z galaxy studies shows no galaxy bias estimates, but only the galaxy correlation lengths r_0 , and the power-law indices of the two point spatial correlation function γ . For these results, we calculate the galaxy

biases in the same manner as Ono et al. (2014) from $b_g = \sigma_{8,\text{gal}}/\sigma_8(z)$, where $\sigma_8(z)$ is a matter fluctuation in spheres of comoving radius of $8 h^{-1}\text{Mpc}$, and $\sigma_{8,\text{gal}}$ is a galaxy fluctuation. The value of $\sigma_{8,\text{gal}}$ is derived with (see eq. 7.72 in Peebles 1993)

$$\sigma_{8,\text{gal}}^2 = \frac{72}{(3-\gamma)(4-\gamma)(6-\gamma)2^\gamma} \left(\frac{r_0}{8 h^{-1}\text{Mpc}} \right)^\gamma. \quad (10)$$

In Figure 8, the galaxy bias estimates for the most of SMGs, DRGs, and pBzKs are higher than the upper limit of our faint ALMA sources. On the other hand, K -selected star-forming galaxies of sBzKs have the halo masses comparable with those of our faint ALMA sources. The UV-selected LBGs and LAEs also have the galaxy bias values similar to our faint ALMA sources. Thus, we find that our faint ALMA sources are not similar to SMGs, DRGs, and pBzK with masses of $\gtrsim 10^{13} M_\odot$ but sBzKs, LBGs, and LAEs with masses $\lesssim 10^{13} M_\odot$ (Figure 8). These clustering results suggest a possibility in a statistical sense that a large fraction of our faint ALMA sources could be mm counterparts of sBzKs, LBGs, and LAEs.

6. MULTI-WAVELENGTH PROPERTIES OF THE FAINT ALMA SOURCES

6.1. Optical-NIR Counterparts

We investigate optical-NIR counterparts of our faint ALMA sources, and characterize the sources with the multi-wavelength properties, especially the optical-NIR colors. We search for the optical-NIR counterparts in the regions of SXDS and A1689 that have rich multi-wavelength data. In these two regions, there are a total of 65 faint ALMA sources; 54 and 11 sources in SXDS and A1689 regions, respectively. For the optical-NIR counterpart studies so far conducted, this is the largest sample of faint mm sources down to ~ 0.02 mJy, while there exist studies, such as ALESS and COSMOS, that use a comparably large but relatively bright sample (Hodge et al. 2013; Scoville et al. 2015).

Table 6 summarizes the multi-wavelength data of SXDS and A1689 used in this study. The multi-wavelength data cover from X-ray to far-infrared (FIR) radiation. In the SXDS region, we use published photometry catalogs in 0.5-10 keV (Ueda et al. 2008), u^* (Foucaud et al. in preparation), B , V , R , i' , z' (Furusawa et al. 2008), J , H , K (UKIDSS DR10; Almaini et al. in preparation), $3.6 - 24 \mu\text{m}$ (Spitzer UKIDSS Ultra Deep Survey; SpUDS), $250 - 500 \mu\text{m}$ (Herschel Multi-tiered Extragalactic Survey; HerMES, Oliver et al. 2012), and 1.4 GHz (Simpson et al. 2006) as well as the photometric redshift (z_{phot}) catalog (Williams et al. 2009). In the A1689 region, we investigate published photometry catalogs of g_{475} , r_{625} , i_{775} , z_{850} , J_{110} , H_{160} (Hubble Source Catalog; HSC), $3.6 - 24 \mu\text{m}$ (Spitzer Enhanced Imaging Products; SEIP), $250 - 500 \mu\text{m}$ (HerMES), and the photometric redshift z_{photo} and spectroscopic redshift z_{spec} catalogs (Limousin et al. 2007; Coe et al. 2010; Diego et al. 2015).

We use the u^* to K (g' to H) band images in the SXDS (A1689) region for the optical-NIR ($0.4 - 2 \mu\text{m}$) counterpart identification, because these data have a good spatial resolution. The optical-NIR counterparts are de-

finned by the criterion that the distance between optical-NIR and ALMA source centers is within a $1''.0$. If an ALMA source meets this criterion in any of optical-NIR bands, we regard that the ALMA source has an optical-NIR counterpart. The $1''.0$ radius is chosen, because the absolute positional accuracy (APA) of $\simeq 1''.0$ is guaranteed in our ALMA data (cf. optical-NIR data for $\lesssim 0''.3$; see, e.g., Furusawa et al. 2008). Regarding the ALMA's APA, the knowledge base page of ALMA Science portal presents that the APA is smaller than the synthesized beam width⁶. Because the synthesized beam widths of our data are $\lesssim 1''.0$, the $1''.0$ radius is applied.

Using the SXDS+A1689 source catalog of the 65 faint ALMA sources, we identify a total of 17 optical-NIR counterparts. Fifteen and two sources are identified in SXDS and A1689 and referred to as S1-15 and A1-2, respectively. Figure 15 shows the postage stamps of these identified sources, and Table 7 summarizes their photometric properties. The photometry values in Table 7 are total magnitudes. The u^* magnitudes are MAG_AUTO values given by our SExtractor photometry. Similarly, $BVR_{ci}'z'$ magnitudes are MAG_AUTO values listed in the Furusawa et al. (2008)'s catalogs. The *Spitzer* photometry values are estimated from the SEIP aperture flux densities with the aperture correction⁷, while the *HST* photometry values (for A1 and A2) are the total magnitudes calculated from MAG_APER values of our SExtractor measurements and the aperture correction⁸. Note that there is an offset of $1''.2$ ($1''.06$) between the flux peaks of the optical-NIR counterpart and S9 (S15) ALMA source. Because S9 and S15 have an extended optical-NIR profile whose major component falls in the ALMA emitting region, the optical-NIR source is selected as a counterpart of the ALMA source.

Because spurious sources are included in the 65 faint ALMA sources, we calculate the real ALMA source number in the SXDS (A1689) region. In the SXDS (A1689) region, we subtract the expected spurious-source number of 31 (5) from the SXDS (A1689) source number of 54 (11), and estimate the real ALMA source number to be 23 (6). The total real ALMA source number in these two regions is 29 ($= 23 + 6$). Thus, the counterpart-identification fraction that is the ratio of the total optical-NIR counterpart ALMA sources to the real ALMA sources is estimated to be 59% ($= 17/29$). We estimate the probability of the chance projection that a foreground or background object is located by chance in the $1''.0$ -radius circle of an ALMA source, and obtain $\sim 10\%$ in the P -value (Downes et al. 1986). Multiplying this probability with the number of optical-NIR counterparts, 17, we expect that ~ 2 objects would be the foreground/background contamination. Even if we include this contamination effect, a half of our faint ALMA sources, 52% ($= [17 - 2]/29$), have an optical-NIR counterpart.

Interestingly, there is a difference of the counterpart-identification fractions between SXDS and A1689 re-

gions, although the depths of the optical-NIR data are comparable in these two regions (27 – 28 mag in optical and 25 – 26 mag in NIR; see Table 6). The counterpart-identification fraction in the SXDS region is 65% ($= 15/23$), while the one in the A1689 region is only 33% ($= 2/6$). Including the 1σ statistical uncertainties, these fractions are $65 \pm 22\%$ and $33 \pm 30\%$ for the SXDS and A1689 regions, respectively. We carefully examine whether this difference is just an artifact originated from, for examples, a systematically high spurious rate and cluster member galaxy obscurations in the cluster region. However, there are no hints of notable artificial effects in the data. Chen et al. (2014) also report a similarly low-identification rate of MIR/radio counterparts in A1689 based on their observations with SMA. It should be noted that the intrinsic mm flux densities of our sources in the A1689 region are $\simeq 0.01 - 0.1$ mJy (magnification corrected) that is about an order of magnitude fainter than those of our sources in the SXDS region, $\simeq 0.1 - 1$ mJy.

There are two possible explanations for the difference between SXDS and A1689. The first explanation is made by the negative k-correction. Due to the faint flux densities, the mm sources of the A1689 would reside at a redshift higher than the SXDS sources on average, since the abundance of the dusty population decreases towards the epoch of the first-generation galaxies. Because the effect of the negative k-correction is significant, the ratio of mm to optical-NIR fluxes is higher for high- z sources than low- z sources. In this case, the counterpart-identification fraction would be small in the A1689 region. The second explanation is the A1689's lensing distortion effects in conjunction with the intrinsic offsets between mm and optical-NIR emitting regions within a galaxy. Chen et al. (2015) report that there is an offset between submm and optical-NIR emitting regions typically by $\sim 0''.4$. If there is an intrinsic $\sim 0''.4$ offset in the source plane of A1689, the image distortion effects of lensing would magnify the offset to $> 1''.0$. We thus estimate the probability that the offsets between mm and optical-NIR sources in the source plane is magnified to $> 1''.0$ in the image plane by Monte-Carlo simulations. We place 100 artificial sources in the source plane of A1689 at around an ALMA source in A1689. The positions of these artificial sources follow the Gaussian distributions whose standard deviation is $0''.4$. Using our mass model, we calculate the offsets between the ALMA source and the artificial sources in the image plane. We repeat this process for 11 ALMA sources in A1689. We find that $\sim 50\%$ of the artificial sources show $> 1''.0$ offsets from the ALMA source in the image plane. Because the number of optical counterparts in A1689 is 2, our simulation results suggest that a total of 4 ($= 2/[50\%]$) optical counterparts should exist in the case of no lensing distortion effects (+the intrinsic offsets). Thus, the true counterpart-identification fraction of A1689 is 67% ($= 4/6$) that is very similar to the counterpart-identification fraction of SXDS ($65 \pm 22\%$). If the lensing distortion effects (+the intrinsic offsets) would provide 2 ($= 4 - 2$) sources whose optical counterparts have an offset from the ALMA sources by $> 1''.0$ in the image plane, we would find such ALMA sources whose optical counterparts are located at the position just beyond $1''.0$ in our data. We refer the distribution of the artificial optical counterparts from our simula-

⁶ The APA is larger than $0''.1$ that is originated from the uncertainties of phase calibrator positions and the baseline lengths of antennas.

⁷ <http://irsa.ipac.caltech.edu/data/SPITZER/docs/irac/iracinstrumenthandbook/29/>

⁸ http://archive.stsci.edu/hst/hsc/help/FAQ/aperture_corrections.txt

tions, and search for potential optical-NIR counterparts whose distances from the ALMA sources are $> 1''.0$. We find such potential optical counterparts in 4 sources of A1689, some of which may be real optical counterparts, and confirm the hypothesis that the combination of the lensing distortion effects and the intrinsic offsets can be the major reason for the difference of the counterpart-identification fractions between the cluster of A1689 and the blank field of SXDS.

Table 7 lists the photometry of the *Spitzer* ($3.6\text{--}24\text{ }\mu\text{m}$) and *Herschel* ($250\text{--}500\text{ }\mu\text{m}$) data. Because the spatial resolutions of the *Spitzer* and *Herschel* data are poor, we determine the *Spitzer* and *Herschel* counterparts by visual inspection that allows sources residing at a position slightly beyond the $1''$ search radius. Although no sources are identified in the *Herschel* bands, about a half of our faint ALMA sources are detected in the *Spitzer* data. These results would indicate that our faint ALMA sources are very high redshift sources ($z > 4$). However, it should be noted that the *Herschel* data can detect dusty starbursts whose SFRs are very high, $> a\text{ few }100M_{\odot}\text{yr}^{-1}$ even at $z \sim 2\text{--}3$.

Here we examine whether we simply miss red spectral energy distribution (SED) objects that are not detected in optical-NIR ($0.4\text{--}2\text{ }\mu\text{m}$) bands but only in *Spitzer* and *Herschel* bands. We search for *Spitzer* and *Herschel* counterparts of our faint ALMA sources with no optical-NIR counterparts, adopting the visual inspection technique described above. We find no *Spitzer* and *Herschel* counterparts that have undetectable optical-NIR fluxes. Again, these results do not suggest that our faint ALMA sources are dusty starbursts.

We cross-match the catalogs of our faint ALMA sources and the radio 1.4 GHz and X-ray 0.5-10 keV sources. We find no counterparts within a $1''.0\text{--}3''.0$ radius around our faint ALMA sources. Thus, our faint ALMA sources have no signatures of AGN.

To summarize these counterpart identification results with the *Spitzer* and *Herschel* as well as radio and X-ray data, there are signs of neither dusty starbursts nor AGNs in our faint ALMA sources. Note that these cross-match analysis is completed only in SXDS because there are no radio and X-ray data available in A1689.

6.2. Lensed ALMA Sources in A1689

We identify two optical counterparts of A1 and A2 that are lensed by the A1689 cluster. The optical image at the position of A1 is presented in Figure 9. There is a small positional offset of $\sim 0''.8$ between the optical and mm emission, but this small difference can be explained by the positional uncertainty of the ALMA image (Section 6.1)⁹.

This optical counterpart of A1 is one of three known multiple images that is dubbed 5.2, while the rest of two multiple images are called 5.1 and 5.3 (Limousin et al. 2007). We investigate our ALMA image at the optical positions of 5.1 and 5.3 sources. In the ALMA image, the 5.1 source is marginally detected at the 3σ level, while the 5.3 source has no signals above the 3σ level. Table

8 summarizes the physical properties of these three multiple images. The difference of mm emissivities between these multiple images is discussed in Section 6.1.

Although the 5.2 source, i.e. A1, does not have a spectroscopic redshift, the redshift of the 5.1 and 5.3 sources is $z = 2.60$ determined by spectroscopy (Richard et al. in preparation, see Limousin et al. 2007). We thus regard that the redshift of A1 is $z = 2.60$. We calculate the intrinsic 1.2 mm flux of A1 from our 1.3 mm data with the flux scaling factor from 1.3 mm to 1.2 mm (Section 3), and obtain 0.020 ± 0.008 mJy that is corrected for the gravitational lensing magnification of $\mu = 22.8$ and the primary beam sensitivity. Chen et al. (2014) report that the 5.1 and 5.3 sources are not detected above the 3σ level by their Submillimeter Array (SMA) $870\text{ }\mu\text{m}$ observations, but only the 5.2 source. Chen et al. (2014) measure the flux of the 5.2 source, and find the intrinsic flux of 5.2 source is 0.085 ± 0.035 mJy at $870\text{ }\mu\text{m}$, which corresponds to 0.033 ± 0.014 mJy at 1.2 mm with the k -correction from $870\text{ }\mu\text{m}$ to 1.2 mm (Section 3). This 1.2 mm flux of 0.033 ± 0.014 mJy is consistent with our measurement of 0.020 ± 0.008 mJy within the 1σ uncertainties.

The optical-NIR counterpart of A2 is identified in the optical bands with a lensing magnification factor of $\mu = 4.9$. The intrinsic 1.2 mm flux of A2 is estimated to be 0.077 ± 0.035 mJy that are corrected for the gravitational lensing magnification and the primary beam attenuation. Neither z_{spec} nor z_{photo} of A2 are available in the literature.

We compare these A1689 sources with optical-NIR counterparts (Table 8) and the previously-known lensed sources, Cosmic Eyelash (e.g., Swinbank et al. 2010) and SMMJ16358 (e.g., Kneib et al. 2004), identified by single-dish observations. Cosmic Eyelash and SMMJ16358 have intrinsic SFRs of ~ 210 and $500M_{\odot}\text{yr}^{-1}$, respectively. These SFRs correspond to 0.5 and 1.3 mJy at 1.2 mm under the assumption of the $SFR - L_{\text{IR}}$ relation (Kennicutt 1998). On the other hand, our optical-NIR counterparts have intrinsic fluxes of $\sim 0.02\text{--}0.08$ mJy at 1.2 mm. Thus, our ALMA study has identified sources with intrinsic fluxes $\gtrsim 10$ times fainter than these lensed sources.

Although there are no optical-NIR counterparts, we find a very strongly lensed source candidate, A3, that shows ALMA flux double peaks dubbed A3a and A3b. The upper panel of Figure 10 shows the ALMA image of A3. The A3 source is very close to the critical line for a $z = 3$ source (Figure 10), and the critical line is located between the double peaks of A3. More quantitatively, we investigate whether these double peaks can be explained by multiple images of a single lensed source behind A1689. Using our mass model, we calculate positions of multiple images made by a lensed source at $z = 2\text{--}6$ (cyan lines in the upper panel of Figure 10). We find that multiple images at $z \sim 3$ reproduce the positions of the double peaks very well. The best-fit redshift is $z = 3.07$, and the magnification factor is very high, 159. The bottom panel of Figure 10 is the HST optical images. No optical counterparts of A3 are found. We summarize the properties of A3 in Table 9.

⁹ There remains a possibility that the offset would be a real positional difference between the optical and mm emitting regions. However, it requires ALMA data analysis for a positional accuracy better than this study.

Table 6
Multi-wavelength Data

Region (N_{counter}) (1)	Telescope/Instrument	Band (5σ limit in mag) (2)	Reference (3)
SXDS (15)	<i>XMM-Newton</i> /EPICs, pn, MOS	0.5-10 keV ($6 - 50 \times 10^{-16}$ erg cm $^{-2}$ s $^{-1}$)	(a)
	CFHT/MegaCam	u^* (27.7)	(b)
	Subaru/Suprime-Cam	B (28.4)	(c)
	Subaru/Suprime-Cam	V (28.0)	(c)
	Subaru/Suprime-Cam	R_c (27.8)	(c)
	Subaru/Suprime-Cam	i' (27.7)	(c)
	Subaru/Suprime-Cam	z' (26.7)	(c)
	UKIRT/WFCAM	J (25.6)	(d)
	UKIRT/WFCAM	H (24.8)	(d)
	UKIRT/WFCAM	K (25.4)	(d)
	<i>Spitzer</i> /IRAC	$3.6\mu\text{m}$ (24.7)	(e)
	<i>Spitzer</i> /IRAC	$4.5\mu\text{m}$ (24.6)	(e)
	<i>Spitzer</i> /IRAC	$5.8\mu\text{m}$ (22.3)	(f)
	<i>Spitzer</i> /IRAC	$8.0\mu\text{m}$ (22.3)	(f)
	<i>Spitzer</i> /MIPS	$24\mu\text{m}$ (18.0)	(f)
	<i>Herschel</i> /SPIRE	$250\mu\text{m}$ (13.8)	(g)
	<i>Herschel</i> /SPIRE	$350\mu\text{m}$ (14.0)	(g)
	<i>Herschel</i> /SPIRE	$500\mu\text{m}$ (13.6)	(g)
	VLA	1.4 GHz (20.0)	(h)
A1689 (2)	<i>HST</i> /ACS	g_{475} (28.6)	(i)
	<i>HST</i> /ACS	r_{625} (28.3)	(i)
	<i>HST</i> /ACS	i_{775} (28.2)	(i)
	<i>HST</i> /ACS	z_{850} (27.8)	(i)
	<i>HST</i> /NICMOS	J_{110} (26.2)	(j)
	<i>HST</i> /WFC3	H_{160} (26.3 – 28.1)	(k)
	<i>Spitzer</i> /IRAC	$3.6\mu\text{m}$ (24.8)	(l)
	<i>Spitzer</i> /IRAC	$4.5\mu\text{m}$ (24.3)	(l)
	<i>Spitzer</i> /IRAC	$5.8\mu\text{m}$ (23.4)	(l)
	<i>Spitzer</i> /IRAC	$8.0\mu\text{m}$ (22.9)	(l)
	<i>Spitzer</i> /MIPS	$24\mu\text{m}$ (19.5)	(l)
	<i>Herschel</i> /SPIRE	$250\mu\text{m}$ (14.0)	(g)
	<i>Herschel</i> /SPIRE	$350\mu\text{m}$ (14.2)	(g)
	<i>Herschel</i> /SPIRE	$500\mu\text{m}$ (13.8)	(g)

Note. — Columns: (1) Name of the region. The number, N_{counter} , in the parentheses indicates the number of the optical-NIR counterparts. (2) Limiting magnitude defined by 5σ sky noise in a circular aperture with a radius of PSF FWHM. (3) Reference or source catalogue: (a) Ueda et al. (2008); (b) Foucaud et al. (in preparation); (c) Furusawa et al. (2008); (d) UKIDSS (O. Almaini et al. in preparation); (e) SEDS (Ashby et al. 2013); (f) SpUDS; (g) HerMES (Oliver et al. 2012); (h) Simpson et al. (2006); (i) Alavi et al. (2014); (j) Bouwens et al. (2009); (k) Bouwens et al. (2015); (l) SEIP.^a

^a<http://irsa.ipac.caltech.edu/data/SPITZER/Enhanced/SEIP/overview.html>

6.3. Color and Luminosity Properties of the Optical-NIR Counterparts

We investigate color (i.e. SED) and luminosity properties of the optical-NIR counterparts, S1-15 and A1-2, to understand the population of the faint ALMA sources with the detectable optical-NIR continuum emission. First of all, we refer the catalog of photo- z estimated from the optical-NIR SEDs (Williams et al. 2009), and find that S11, S12, S15 have photo- z values of $1.54^{+0.08}_{-0.02}$, $1.57^{+0.07}_{-0.02}$, and $1.45^{+0.03}_{-0.02}$, respectively. However, the photo- z values of the S4 and S6 sources are $0.77^{+0.23}_{-0.03}$ and $0.67^{+0.01}_{-0.02}$, respectively. We thus regard that the S4 and S6 sources reside at low redshift ($z < 1$), and find that $\sim 10\%$ ($= 2/17$) optical-NIR counterparts are low- z objects. Because the majority of mm sources are thought to be high- z galaxies and AGNs (Casey et al. 2014), the rest of 15 ($= 17 - 2$) optical-NIR counterparts are candidates of high- z galaxies. We thus compare colors and luminosities of these high- z galaxy candidates with those of high- z sources. The major high- z populations are SMGs, LBGs (including BX/BM), DRGs, BzKs, LAEs, and AGNs. Since the SMGs, DRGs, and LAEs generally have weak optical continua that cannot

be reliably compared with our optical-NIR counterparts, we focus on the comparisons with LBGs (BX/BM) and BzKs.

6.3.1. Comparison with the LBG BX/BM Populations

The BX and BM galaxies, generally included in the LBG population, reside in the redshift ranges of $2.0 \lesssim z \lesssim 2.5$ and $1.5 \lesssim z \lesssim 2.0$, respectively (Steidel et al. 2004). Similarly, there are LBGs at $z \sim 3$. These galaxies are defined by the selection criteria of $U_n - G$ and $G - R$ colors. We apply these color selection criteria to our optical-NIR counterparts, but the photometry bands of our data are different from the U_n , G and R bands. Following the procedures of Ly et al. (2011), we alternatively use a color set of $U - BV$ and $BV - R_c i'$. The BV and $R_c i'$ photometry are defined by

$$BV = -2.5 \log \left[\frac{x_1 f_B + (1 - x_1) f_V}{3630 \mu Jy} \right],$$

$$R_c i' = -2.5 \log \left[\frac{x_2 f_R + (1 - x_2) f_{i'}}{3630 \mu Jy} \right], \quad (11)$$

where f_X is the flux density per unit frequency (erg s $^{-1}$ cm $^{-2}$ Hz $^{-1}$) in a band 'X' corresponding to B , V , R_c ,

Table 7
Photometry of the Optical-NIR Counterparts

ID	u^*	B	V	R_c	i'	z'	J	H	SXDS	$3.6\mu\text{m}$	$4.5\mu\text{m}$	$5.8\mu\text{m}$	$8.0\mu\text{m}$	$24\mu\text{m}$	$250\mu\text{m}$	$350\mu\text{m}$	$500\mu\text{m}$
									K								
S1	...	24.46	24.24	23.85	23.52	22.88	20.02	19.94	20.11	20.12	> 18.56	> 14.35	> 14.55	> 14.15
S2	...	25.91	26.18	26.59	26.71	25.01	> 25.27	> 25.16	> 22.85	> 22.81	> 18.56	> 14.35	> 14.55	> 14.15
S3	27.24	26.69	26.35	25.63	25.29	25.25	24.80	24.43	24.41	> 25.27	> 25.16	> 22.85	> 22.81	> 18.56	> 14.35	> 14.55	> 14.15
S4	25.76	25.61	25.30	25.00	24.47	24.05	23.21	22.92	22.66	21.68	21.84	> 22.85	> 22.81	> 18.56	> 14.35	> 14.55	> 14.15
S5	26.31	25.11	24.70	24.76	24.58	24.75	24.53	24.05	24.22	> 25.27	> 25.16	> 22.85	> 22.81	> 18.56	> 14.35	> 14.55	> 14.15
S6	25.69	24.84	23.76	22.79	21.96	21.55	20.81	20.42	20.08	19.61	20.06	19.95	20.24	> 18.56	> 14.35	> 14.55	> 14.15
S7	> 28.23	27.14	27.42	27.30	27.32	26.62	> 26.18	> 25.31	> 25.94	> 25.27	> 25.16	> 22.85	> 22.81	> 18.56	> 14.35	> 14.55	> 14.15
S8 [†]	24.57	> 28.93	> 28.56	> 28.33	> 28.24	> 27.22	> 26.18	> 25.31	> 25.94	> 25.27	> 25.16	> 22.85	> 22.81	> 18.56	> 14.35	> 14.55	> 14.15
S9 ^{††}	> 28.23	25.30	23.86	22.96	21.63	20.93	20.24	20.22	20.45	20.40	20.78	20.46	> 22.81	> 18.56	> 14.35	> 14.55	> 14.15
S10	> 28.23	26.68	26.25	26.25	25.65	25.07	25.90	24.60	25.67	> 25.27	> 25.16	> 22.85	> 22.81	> 18.56	> 14.35	> 14.55	> 14.15
S11	26.00	25.14	24.66	24.53	24.02	23.62	22.36	21.76	21.26	19.91	19.69	19.31	19.51	15.95	> 14.35	> 14.55	> 14.15
S12	23.45	23.22	22.96	22.94	22.65	22.45	21.55	21.18	20.88	19.89	19.66	19.35	19.62	16.66	> 14.35	> 14.55	> 14.15
S13	> 28.23	> 28.93	28.50	> 28.33	> 28.24	> 27.22	> 26.18	> 25.31	25.22	22.55	22.73	22.33	> 22.81	> 18.56	> 14.35	> 14.55	> 14.15
S14	> 28.23	25.96	26.09	25.68	> 28.24	> 27.22	> 26.18	> 25.31	> 25.94	> 25.27	> 25.16	> 22.85	> 22.81	> 18.56	> 14.35	> 14.55	> 14.15
S15	23.87	23.49	23.40	23.08	22.84	22.42	21.72	21.25	21.16	20.27	20.12	20.32	19.89	> 18.56	> 14.35	> 14.55	> 14.15
Abell 1689																	
ID	g_{475}	r_{625}	i_{775}	z_{850}	J_{110}	H_{160}	...	$3.6\mu\text{m}$	$4.5\mu\text{m}$	$5.8\mu\text{m}$	$8.0\mu\text{m}$	$24\mu\text{m}$	$250\mu\text{m}$	$350\mu\text{m}$	$500\mu\text{m}$
A1	26.61	25.78	24.79	25.36	24.29	23.55	...	18.25	18.45	18.72	19.10	16.94	> 14.55	> 14.75	> 14.35
A2	27.35	26.28	25.84	25.59	> 26.75	24.36	...	> 25.35	> 24.85	> 23.95	> 23.45	> 20.05	> 14.55	> 14.75	> 14.35

Note. — The u^* magnitudes are MAG_AUTO values given by our SExtractor photometry. Similarly, $BVR_c i' z'$ magnitudes are MAG_AUTO values listed in the Furusawa et al. (2008)'s catalogs. The *Spitzer* photometry values are total magnitudes estimated from the SEIP aperture flux densities with the aperture correction, while the *HST* photometry values (for A1 and A2) are the total magnitudes calculated from MAG_APER values of our SExtractor measurements. The aperture corrections for the *Spitzer* and *HST* photometry are provided by the *Spitzer* and *HST* websites, respectively (see text). The lower limits correspond to the 3σ levels. The S1 and S2 objects are not observed in u^* band and JHK bands.

[†] The secure photometry cannot be carried out due to the blending with a bright neighboring objects for the B-500 μm bands. See Figure 15.

^{††} The positions of the optical-NIR counterpart are far from the ALMA source center by $\sim 1''2$.

Table 8
Multiple Images at $z = 2.60$ with the ALMA Counterpart

ID (L07) (1)	ID (This work) (2)	R.A. (J2000) (3)	Decl. (J2000)	$S_{1.3\text{mm}}^{\text{obs}}$ (mJy) (4)	$S_{1.3\text{mm}}^{\text{corr}}$ (mJy) (5)	$S_{1.2\text{mm}}^{\text{corr}}$ (mJy) (6)	g_{475}	r_{625} i_{775} (mag _{AB}) (7)	z_{850}	μ (8)
5.1	...	13:11:29.064	−1:20:48.64	$0.18 \pm 0.06^\dagger$	0.049 ± 0.021	0.067 ± 0.029	26.29	25.53 25.37	25.17	5.7
5.2	A1	13:11:29.224	−1:20:44.24	0.30 ± 0.06	0.015 ± 0.006	0.020 ± 0.008	26.61	25.78 25.58	25.36	22.8
5.3	...	13:11:34.120	−1:20:20.96	< 0.28	< 0.093	< 0.13	26.61	25.85 25.85	25.60	3.0

Note. — (1) and (2) ID names given in Limousin et al. (2007) (L07) and this work, respectively. (3) R.A. and Decl. in the optical data. (4) Peak flux density SExtractor measurement (Section 3.1) with the primary beam correction. If no significant 1.32 mm fluxes are detected at the optical source positions, three sigma upper limits are presented. (5) Observed flux density at 1.32 mm on the uv-taper image that are measured by 2D Gaussian-fitting routine of *imfit* in CASA with the primary beam correction. The magnification uncertainty (Section 3.5) is included in the error. (6) Source flux density at 1.2 mm with the flux scaling from 1.32 mm to 1.2 mm (Section 3). (7) Total magnitudes in the *HST*/ACS bands. (8) Magnification factor at the peak of the optical flux.

† Marginal detection of the 3σ level that is below our source selection limit for the cluster data ($> 3.9\sigma$; see Section 3.2).

Table 9
Very Strongly Lensed Source Candidate

ID (1)	R.A. (J2000) (2)	Decl. (J2000)	$S_{1.3\text{mm}}^{\text{obs}}$ (mJy) (3)	$S_{1.3\text{mm}}^{\text{corr}}$ (mJy) (4)	$S_{1.2\text{mm}}^{\text{corr}}$ (mJy) (5)	g_{475}	r_{625} i_{775} (mag _{AB}) (6)	z_{850}	μ (7)
A3	13:11:26.897	−1:20:32.02	0.24 ± 0.06	0.0015 ± 0.0007	0.0020 ± 0.0010	> 28.56	> 28.33 > 28.24	> 27.22	159.5

Note. — (1) – (7) correspond to (2) – (8) in Table 8. These values are for the A3a component (Figure 10). Because A3a and A3b are confused in the uv-taper image, these fluxes are obtained on the image without uv-taper.

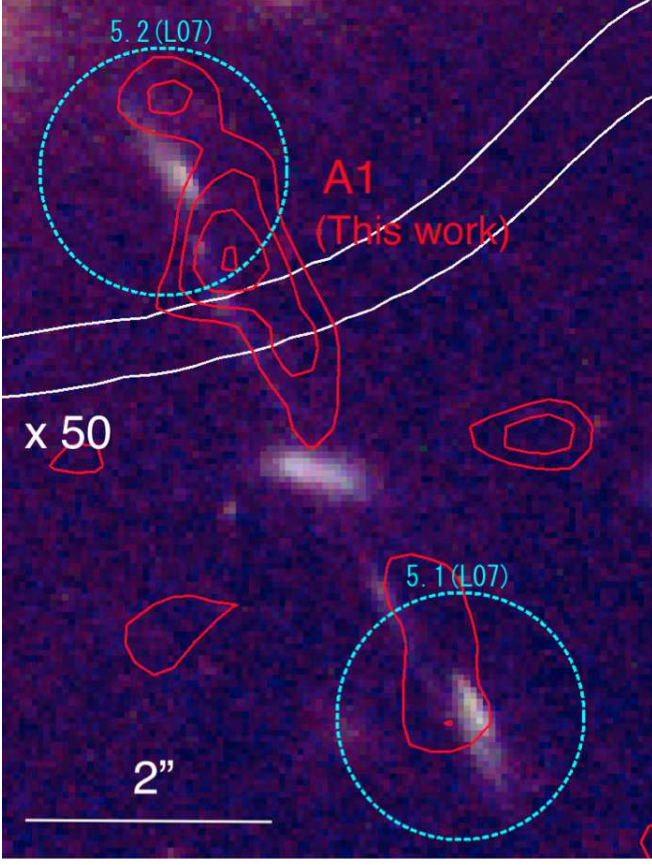


Figure 9. False-color image of A1. The used images and color assignment are the same as Figure 1. The center of the cyan circles pinpoint the positions of the 5.1 and 5.2 sources, which are two of the multiple images of the galaxy at $z_{\text{spec}} = 2.60$ (Limousin et al. 2007; Coe et al. 2010). The radius of the cyan circle is $1''.0$ that corresponds to the search radius for the counterpart identifications. The red contours show the ALMA 1.3 mm emission at the 2, 3, 4, and 5 σ levels. The white curves represent the lines for the lensing magnification of $\mu = 50$.

and i' . The coefficients of x_1 and x_2 are 0.314 and 0.207, respectively. With these photometric relations and the selection colors (Steidel et al. 2004), the color criteria of BX objects are re-written as

$$\begin{aligned} BV - R_{ci}' &\geq -0.2, \\ U - BV &\geq BV - R_{ci}' + 0.23, \\ BV - R_{ci}' &\leq 0.2(u - BV) + 0.4, \\ U - BV &\leq BV - R_{ci}' + 1.0. \end{aligned} \quad (12)$$

Similarly, the criteria of BM objects are

$$\begin{aligned} BV - R_{ci}' &\geq -0.2, \\ U - BV &\geq -0.1, \\ BV - R_{ci}' &\leq -0.382(U - BV) + 0.853, \\ BV - R_{ci}' &\leq 0.70(U - BV) + 0.280, \\ U - BV &\geq BV - R_{ci}' + 0.23. \end{aligned} \quad (13)$$

We compare these color criteria with our optical-NIR counterparts. Among the 17 optical-NIR counterparts, 10 are observed with the photometric system of $u^*BV R_{ci}'$ necessary for the comparison. Removing the 2 obvious low- z objects of S4 and S6, we use 8 optical-NIR

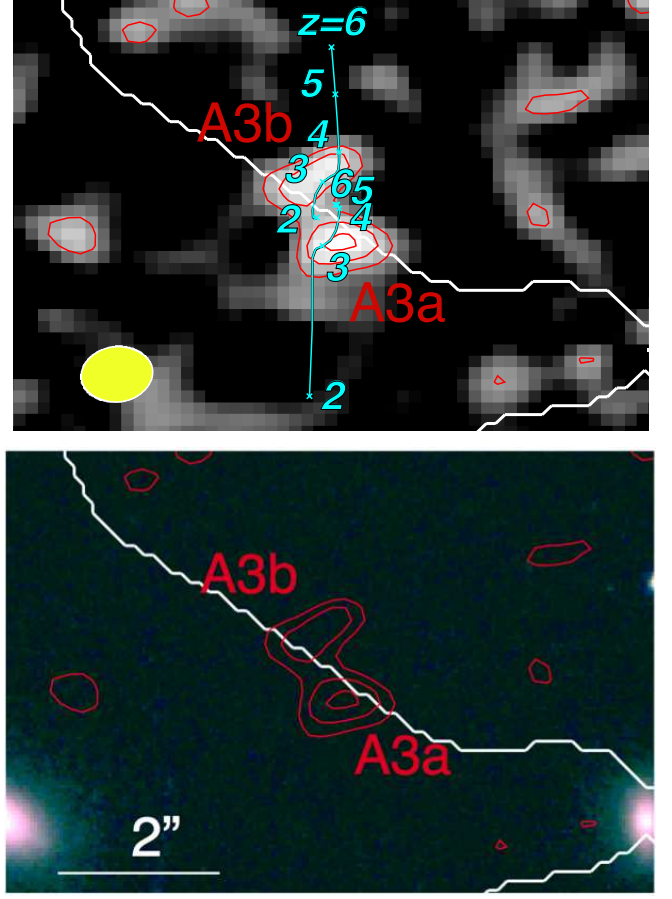


Figure 10. Very strongly lensed source candidate, A3, found in A1689. The red contours show the ALMA 1.3 mm emission at the 2, 3, 4 σ levels. The white curves denote the critical lines for a $z = 3$ source that are estimated with our mass model. *Top:* ALMA continuum image of A3. The cyan tracks show the positions of multiple images for lensed sources at $z = 2, 3, 4, 5$, and 6 that are predicted with our mass model. The ALMA multiple image positions (red contours; A3a and A3b) are well reproduced by a lensed source at $z \sim 3$. *Bottom:* False-color image of HST optical data showing the same region as the top panel. The used images and color assignment are the same as Figure 1. No optical counterparts of A3 are identified.

counterparts. Figure 11 displays the two color diagram of these 8 sources with the color selection criteria. Six sources fall in or near the selection windows of $z \sim 2$ BX/BM or $z \sim 3$ LBGs, where we include S11 source at the border of the selection window. The S9 source is placed at the upper right corner of Figure 11. These colors of the S9 source are similar to $z \gtrsim 4$ LBGs (see, e.g., Steidel et al. 2003). It is likely that S9 source is a LBG at $z \gtrsim 4$. On the other hand, S3 clearly escapes from the selection windows. We thus find that 7 out of 8 optical-NIR counterparts are have colors consistent with either $z \sim 2$ BX/BM or $z \gtrsim 3$ LBGs. Including the two low- z objects of S4 and S6 sources, 70% ($= 7/[8 + 2]$) of the optical-NIR counterparts meet the LBG (BX/BM) color criteria. We then compare magnitudes of the 10 optical-NIR counterparts with the known $z \sim 2$ BX/BM and $z \gtrsim 3$ LBGs, omitting u^* magnitudes that would include a Lyman break whose central wavelength is very sensitive to a source redshift. We find that all of the 10 optical-NIR sources have R_c magnitudes in the range of

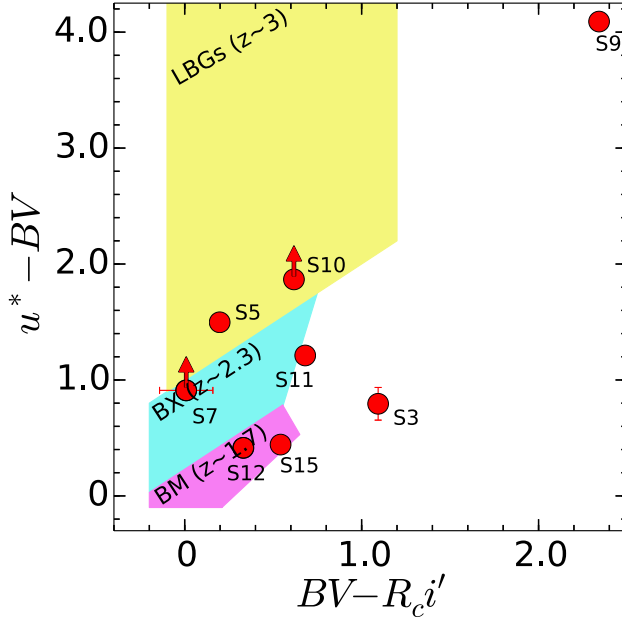


Figure 11. Two-color diagram for our optical-NIR counterparts. The cyan and magenta-shaded regions are the BX and BM selection windows that are defined in the $BV - R_c i'$ and $u^* - BV$ color plane (Ly et al. 2011). The BX and BM galaxies reside at $z \simeq 2 - 2.5$ and $z \simeq 1.5 - 2.0$, respectively. The yellow shades indicate the approximate region of the selection window for $z \simeq 3$ LBGs (Steidel et al. 2003), where we assume that the original photometry of U_n , G and R bands are roughly the same as those of our u^* , B , and R_c bands, respectively.

23 – 27 mag (Table 7) that is typical brightness of $z \sim 2$ BX/BM and $z \gtrsim 3$ LBGs (Steidel et al. 2003, 2004). We thus conclude that a majority ($\sim 70\%$) of the 10 optical-NIR counterparts belong to LBG (BX/BM) population.

6.3.2. Comparison with the BzK Populations

In contrast with BX/BM galaxies and LBGs, the BzK galaxy population includes not only blue star-forming galaxies, but also moderately reddened dust-poor star-forming galaxies (a.k.a sBzK) and passive galaxies (a.k.a pBzK) at $1.4 \lesssim z \lesssim 2.5$ (Daddi et al. 2004). We compare the color criteria of the BzK population with our optical-NIR counterparts. There are 10 out of the 17 optical-NIR counterparts that are located in the SXDS region with the photometric measurements of B , z' , and K bands (Table 7).¹⁰ Removing the 2 obvious low- z objects of S4 and S6, we use 8 optical-NIR counterparts for the comparison.

Because the photometry system of ours (SXDS) is different from that of the BzK studies (Daddi et al. 2004), we again apply corrections to the color selection criteria for BzK galaxies, which are suggested by Yuma et al. (2012),

$$\begin{aligned} (B - z)_{\text{Daddi+04}} &= (B - z)_{\text{SXDS}} + 0.3, \\ (z - K)_{\text{Daddi+04}} &= (z - K)_{\text{SXDS}} + 0.1. \end{aligned} \quad (14)$$

Figure 12 presents the $B - z$ and $z - K$ colors of the 8 optical-NIR counterparts. We find that 5 out of the 8

¹⁰ Note that the A1689 region misses K band photometry critical for the BzK selection.

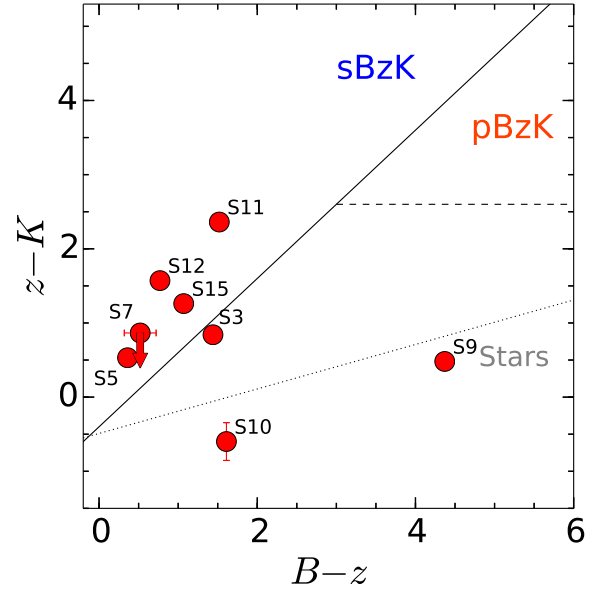


Figure 12. Two-color diagram of the BzK galaxy selection in the SXDS photometry system. The red circles denote the 7 optical-NIR counterparts. Star-forming galaxies at $z \simeq 1.4 - 2.5$, called sBzK galaxies, are selected in the region beyond the solid line defined by $(z - K) - (B - z) \geq -0.2$. The pBzK galaxies, passively evolving galaxies at $z \simeq 1.4 - 2.5$, are selected in the triangular region defined with the solid and dashed ($z - K > 2.5$) lines at the upper right corner. Galactic stars fall in the region below the dotted line (See also Daddi et al. 2004; Yuma et al. 2012).

optical-NIR counterparts meet the color criteria of sBzK, while the rest of the three sources, S3, S9 and S10, have colors different from sBzK or pBzK galaxies whose redshift range is $z \simeq 1.4 - 2.5$. Because S3 also shows the colors different from those of BX/BM galaxies and LBGs (Section 6.3.1), S3 would reside at $z \lesssim 1.4$ that is out of the BzK redshift window. Although the colors of S9 and S10 are similar to those of stars, in Section 6.3.1, the BX/BM galaxy and LBG selections suggest these two sources have colors consistent with $z \gtrsim 3$ galaxies. Thus, S9 and S10 would be galaxies at $z \gtrsim 3$ that escape from the BzK redshift window. In this way, we confirm that the results of the BzK selection are consistent with those of BX/BM galaxies and LBGs. In summary, including the two low- z objects of S4 and S6 sources, we find that $50\% (= 5/[8+2])$ of the optical-NIR counterparts are sBzK galaxies at $z \simeq 1.4 - 2.5$. We then compare magnitudes of these optical-NIR counterparts (Table 7), and find that the optical and NIR magnitudes are comparable with the sBzK galaxies (Daddi et al. 2004).

6.3.3. Comparison with the AGN Population

Six counterparts of S1, S6, S11, S12, S15, and A1 are detected in the mid IR of 8 and 24 μm bands. Because mid-IR bright objects are prominent candidates of AGN that have strong hot-dust emission, we compare colors of the six mid-IR bright counterparts and a typical AGN (Mrk 231) as well as a starburst (Arp 220). Figure 13 shows the colors of the five mid-IR bright counterparts, Mrk 231, and Arp 220 in the diagnostic color diagram of $S_{8.0\mu\text{m}}/S_{4.5\mu\text{m}}$ vs. $S_{24\mu\text{m}}/S_{8.0\mu\text{m}}$ that separates AGN

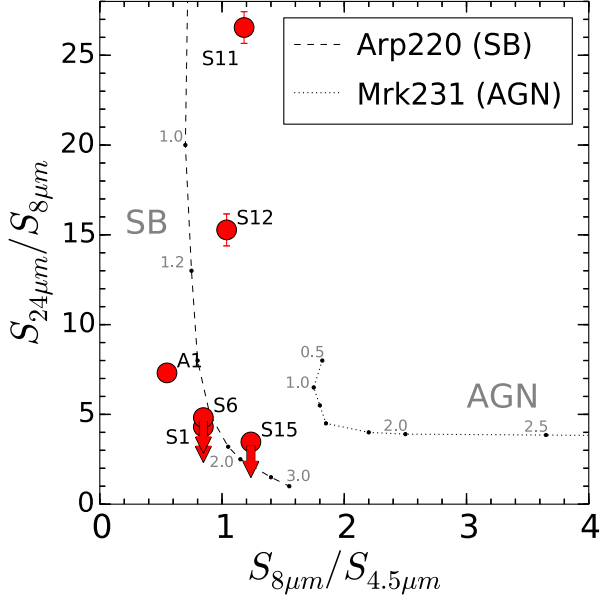


Figure 13. Color-color diagram for the AGN diagnostics. The red circles and upper limits are our five mid-IR bright counterparts. The dotted and dashed lines present the color tracks of Mrk 231 (AGN) and Arp 220 (SB), respectively, that are redshifted from $z \simeq 0.5$ to 3.0 . The numbers labeled to the lines represent the redshifts.

and starburst (SB) populations (Ivison et al. 2004). In Figure 13, the dashed and dotted lines indicate the color tracks of Mrk 231 and Arp 220 in the redshift range of $0.5 - 3.0$ that is taken from Figure 4 of Ivison et al. (2004). All of our five mid-IR bright counterparts are placed near the color track of Arp 220, and far from the one of Mrk 231, which suggest that these six counterparts are not AGN but starbursts.

6.3.4. IRX- β Relation

To evaluate the SED properties quantitatively, we calculate the infrared-to-UV luminosity ratio $\text{IRX} (\equiv L_{\text{IR}}/L_{1600})$ and the rest-frame UV continuum slope β for 6 faint ALMA sources of S4, S6, S11, S12, S15, and A1 that have spectroscopic or photometric redshifts. Here L_{IR} is the integrated infrared flux density defined in a range of rest-frame $8-1000 \mu\text{m}$. The β values are estimated with two broadband magnitudes, m_1 and m_2 :

$$\beta = -\frac{m_1 - m_2}{2.5 \log(\lambda_c^1/\lambda_c^2)} - 2, \quad (15)$$

where λ_c^1 and λ_c^2 are the central wavelengths of the two broadband filters. We use $(m_1, m_2) = (u^*, B)$, (u^*, B) , (V, i') , (V, i') , (V, i') , (r_{625}, z_{850}) for S4, S6, S11, S12, S15, and A1, respectively. These IRX and β values are shown in Figure 14, together with those of nearby (U)LIRGs and optically selected star-forming galaxies at $z \sim 2$. In Figure 14, we also plot the 5.1 source of the multiple image (Table 8) that is marginally detected (3σ). For the lensed sources of A1 and 5.1, we assume that the positional offsets between the submm and optical sources are real, and use the lensing magnification values estimated at the submm (optical) source positions to derive the intrinsic submm (optical) luminosities.

In Figure 14, all of the six faint ALMA sources fall in the region nearly-enclosed by the Calzetti and SMC law curves. The six faint ALMA sources are placed clearly below the (U)LIRGs that have large IRX values at a given β . The clear difference between the faint ALMA sources and (U)LIRGs suggests that the faint ALMA sources are not miniature (U)LIRGs with infrared luminosities fainter than (U)LIRGs by 1–2 order(s) of magnitude. Note that these results are based on the 59% of the faint ALMA sources with the optical-NIR counterparts. The rest of the 41% of the faint ALMA sources that have no optical-NIR counterparts could have IRX values as high as those of (U)LIRGs, because these sources have low L_{1600} values that are suggested by the fact of no optical-NIR counterparts.

These 6 faint ALMA sources are composed of 4 high- z sources (S11, S12, S15, and A1) and 2 low- z sources (S4 and S6), where we define high- z and low- z by $z \geq 1$ and $z < 1$, respectively. Four high- z sources have the IRX- β relation similar to those of optically selected star-forming galaxies at $z = 2$ (Reddy et al. 2012). One low- z source of S4 is also placed at the region of $z = 2$ optically selected galaxies in Figure 14, while the other low- z source of S6 has large IRX and β values. It implies that majority of high- z sources are similar to $z = 2$ optically selected galaxies, but that low- z sources would be widely distributed in the IRX- β plot.

Figure 14 shows that the multiple images of 5.2 (i.e. A1) and 5.1 have similar IRX- β values. This fact confirms that these sources are multiple images of a single high- z source.

6.3.5. What are the Optical-NIR Counterparts of the Faint ALMA Sources?

We summarize the results of Sections 6.3.1-6.3.3 in Table 10. We find, in Sections 6.3.1 and 6.3.2, that 7 out of the 10 optical-NIR counterparts (including the low- z galaxies) meet the color criteria of BX/BM LBG and sBzK galaxy populations (see Table 10), and that the magnitudes of the counterparts are consistent with these populations. The rest of the three counterparts are low- z objects (2 objects) and probably the foreground/background object of the chance projection (1 object; Section 6.1). These results suggest that not all but the majority of the optical-NIR counterparts of our faint ALMA sources belong to the sBzKs and BX/BM LBGs populations. Moreover, the optical-NIR counterparts show neither AGN nor (U)LIRG signatures (Sections 6.3.3 and 6.3.4).

We thus conclude that the majority of our faint ALMA sources with a detectable optical continuum (~ 25 mag) are UV bright star-forming galaxies of BX/BM LBGs and sBzKs with no AGN. This conclusion is supported by the clustering analysis results in Section 5 that presents a weak clustering signal of $b_g < 3.5$ comparable to those of LBGs and sBzKs.

Note that we find the optical-NIR counterparts in 59% of our faint ALMA sources (Section 6.1). In other words, we understand that roughly about a half of the faint ALMA sources are LBGs and sBzKs. For the remaining half of the faint ALMA sources, the physical origin is unclear. Our study identifies a new issue of faint ALMA sources that should be addressed in the future studies.

Table 10
Properties of our Optical-NIR Counterparts

ID	R.A. (J2000)	Decl. (J2000)	λ_{obs} (mm) (1)	$S_{\lambda_{\text{obs}}}^{\text{obs}}$ (mJy) (2)	$S_{1.2\text{mm}}^{\text{corr}}$ (mJy) (3)	z_{photo} (4)	z_{spec} (5)	sBzK (6)	pBzK (7)	BX/BM+LBG (8)	AGN (9)
S1	34.612686	-4.583063	1.22	0.36 ± 0.07	0.43 ± 0.09	N
S2	34.613739	-4.588505	1.22	0.31 ± 0.09	0.31 ± 0.10
S3	34.437805	-5.494339	1.03	0.056 ± 0.015	0.032 ± 0.010	N	N	N	...
S4	34.446648	-5.007715	1.26	0.047 ± 0.014	0.044 ± 0.016	$0.77^{+0.23}_{-0.03}$
S5	34.446007	-5.008159	1.26	0.049 ± 0.014	0.050 ± 0.017	Y	N	Y	...
S6	34.387825	-5.220457	1.25	0.41 ± 0.11	0.42 ± 0.13	$0.67^{+0.01}_{-0.02}$	N
S7	34.411190	-4.745051	1.23	0.30 ± 0.08	$0.14 \pm 0.09^{\dagger}$	Y'	N	Y'	...
S8 ^a	34.305553	-5.067293	1.30	0.29 ± 0.07	0.22 ± 0.09
S9	34.194702	-5.056259	1.25	0.43 ± 0.12	0.39 ± 0.15	N	N	Y'	...
S10	34.197121	-5.059778	1.25	0.31 ± 0.08	0.37 ± 0.10	N	N	Y'	...
S11 ^b	34.442795	-4.911066	1.23	0.53 ± 0.10	0.56 ± 0.11	$1.54^{+0.08}_{-0.02}$...	Y	N	Y'	N
S12	34.441357	-4.912045	1.23	0.32 ± 0.09	0.29 ± 0.09	$1.57^{+0.07}_{-0.02}$...	Y	N	Y	N
S13	34.747295	-4.858103	1.25	0.37 ± 0.10	0.26 ± 0.11
S14	34.274231	-4.860201	1.30	0.32 ± 0.09	0.43 ± 0.12
S15	34.587593	-5.318766	1.25	0.32 ± 0.09	0.21 ± 0.10	$1.45^{+0.03}_{-0.02}$...	Y	N	Y	N
A1 ^c	197.871590	-1.345783	1.32	0.30 ± 0.06	$0.020 \pm 0.008^{\dagger\dagger}$...	2.60	N
A2	197.869086	-1.337143	1.32	0.31 ± 0.08	$0.077 \pm 0.033^{\dagger\dagger}$

Note. — (1): Wavelength in the observed frame. (2): Peak flux density of the SExtractor measurement (Section 3.1) with the primary beam correction at the observed wavelength. (3): The best-estimate source flux density at 1.2 mm. The source flux is estimated with the 2D Gaussian-fitting routine of *imfit* in CASA (Section 3.4) with the primary beam correction and the flux scaling to 1.2 mm (Section 3). For A1 and A2 sources, the lensing magnification corrections are also applied. The lensing magnification factors are estimated at the ALMA flux peak positions of A1 and A2. (4): Photometric redshift estimated by Williams et al. (2009). (5): Spectroscopic redshift obtained by Limousin et al. (2007). (6), (7), (8), and (9): "Y" indicates the objects that meet the color selection criteria of sBzK, pBzK, BX/BM, and AGN populations, respectively. "N" represents the sources escaping from the color space of the selection criteria. "Y'" is presented for the sources having colors consistent with the populations.

[†] The photometry of *imfit* may be biased, due to the systematic noise. The SExtractor peak flux measurement suggests 0.32 ± 0.08 mJy.

^{††} The magnification uncertainty (Section 3.5) is also included in the error.

^aSame as the AS2 source in Hatsukade et al. (2015)

^bSame as the AS4 source in Hatsukade et al. (2015)

^cSame as the Chen-5 source in Chen et al. (2014)

7. SUMMARY

In this paper, we identify 133 faint 1.2-mm continuum sources with a flux density of $0.02 - 1$ mJy in the fifty blank-field and one cluster, Abell 1689, maps taken by ~ 120 deep ALMA Band 6/7 pointings. This is the large faint source sample reaching 0.02 mJy, which is drawn from our deep ALMA projects and the complete archive search for the deep ALMA data that are open for public by 2015 June. Using this large sample of the faint 1.2 mm sources, we derive the 1.2 mm number counts and discuss the faint-source contribution to the EBL. We then investigate the physical origin of these faint 1.2 mm sources by the statistical technique of clustering analysis and the individual-source approach of optical-NIR counterparts. The major results of this paper are summarized below.

1. We derive the 1.2-mm number counts in a flux density range of $0.02 - 1$ mJy. Our number counts are consistent with the previous ALMA and single-dish lensing results, and largely push the flux density limit down to 0.02 mJy. We find that the number counts are well represented by the Schechter function at $\gtrsim 0.02$ mJy, combining the faint and bright number counts from our and the previous studies, respectively.
2. We estimate the total integrated 1.2 mm flux density with the derived number counts, and obtain $22.9^{+6.7}_{-5.6}$ Jy deg^{-2} down to the flux limit of S_{limit} . This integrated 1.2 mm flux density corresponds to $104^{+31}_{-25}\%$ of the EBL measured by COBE ob-

servations. Because we reach $\sim 100\%$ of the EBL-resolved fraction at ~ 0.02 mJy within the errors that are mainly originated from the COBE EBL estimates, the major 1.2 mm EBL contributors are sources with $\gtrsim 0.02$ mJy. In other words, 1.2 mm sources with a flux density below ~ 0.02 mJy make a negligibly small contribution to the EBL. These results suggest a possibility that there is a flattening and/or truncation in the number counts at the very faint flux density regime of $\lesssim 0.02$ mJy.

3. We perform the counts-in-cells analysis for clustering properties of our faint ALMA sources, assuming that these sources reside at $z \sim 1 - 4$. We obtain an upper limit of the galaxy bias $b_g < 3.5$ that is smaller than those of massive galaxy populations of DRGs and SMGs. This upper limit is comparable with the galaxy bias values of UV-bright sBzK and LBG populations.
4. We search for optical-NIR counterparts of our faint ALMA sources located in two regions of SXDS and Abell 1689 that have deep optical-NIR images and the various multi-wavelength data. We identify 17 optical-NIR counterparts, and find that 59% of our faint ALMA sources have the counterparts with the detectable ($m \lesssim 28$ mag) optical-NIR continuum. Neither X-ray nor radio counterparts are found in any of our faint ALMA sources, and the mid-IR diagnostics indicates that there are no AGN activities in these sources. We apply the

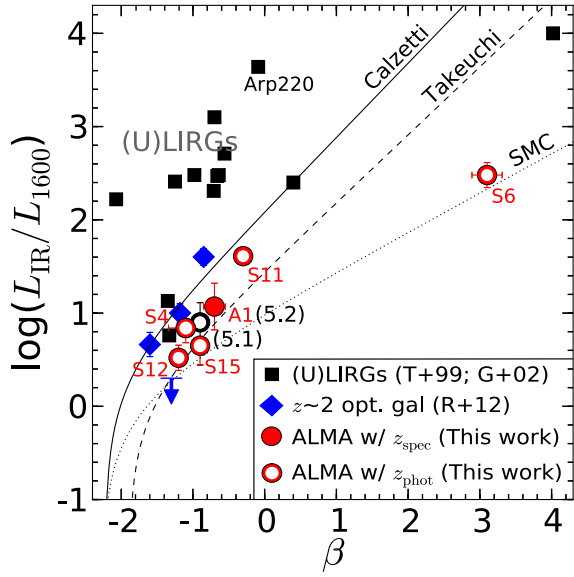


Figure 14. Infrared-to-UV luminosity ratio IRX as a function of the UV slope β . The red filled circle is the spectroscopically-confirmed A1 (5.2) source at $z_{\text{spec}} = 2.60$. The red open circles denote the faint ALMA sources with the photometric redshifts. The open black circle is the 5.1 source of the A1 multiple image system that is marginally detected in the ALMA data (Table 8). The blue diamonds (arrow) represent(s) the measurements (the upper limit) of the $z \sim 2$ optically-selected galaxies obtained by the stacking analysis (Reddy et al. 2012). The black squares indicate nearby (U)LIRGs (Trentham et al. 1999; Goldader et al. 2002). The solid, dashed, and dotted curves denote the IRX- β relation of the extinction curves for the Calzetti law (Meurer et al. 1999), the updated Calzetti law (Takeuchi et al. 2012), and the SMC law (Bouchet et al. 1985). For the Calzetti law curve, we shift the original relation of the Calzetti law (Meurer et al. 1999) by +0.24 dex, because Meurer et al. (1999) define their infrared luminosities at $40 - 120 \mu\text{m}$ that is different from our definition ($8 - 1000 \mu\text{m}$).

color selection criteria of BX/BM LBGs, sBzKs, and pBzKs for our optical-NIR counterparts with a photometric data set necessary for the color selections. We find that a majority of these optical-NIR counterparts have colors meeting the BX/BM LBG and sBzK criteria, and that their magnitudes are comparable to the BX/BM LBGs and sBzKs. Because 59% of our faint ALMA sources have the detectable optical-NIR counterparts, we conclude that about a half of faint ALMA sources are BX/BM LBGs and sBzKs that are high- z galaxies with a star-formation rate and dust extinction much smaller than SMGs. Moreover, the IRX- β relation plot indicates that the optical-NIR counterparts of our faint ALMA sources are clearly different from (U)LIRGs, and that faint ALMA sources are not miniature (U)LIRGs simply scaled down with the infrared brightness.

ACKNOWLEDGEMENTS

We are grateful to Akifumi Seko and Koji Ohta for providing us their reduced data, and Bunyo Hatsukade for giving us helpful advice on analyzing the data and send-

ing their results. We also thank Ryohei Kawabe, Kotaro Kohno, Soh Ikarashi, Kirsten K. Knudsen, Chian-Chou Chen, and Ian Smail for useful information, comments, and discussions. We appreciate the support of the staff at the ALMA Regional Center, especially Kazuya Saigo and Bunyo Hatsukade. This paper makes use of the following ALMA data: ADS/JAO.ALMA#2011.0.00115.S, #2011.0.00232.S, #2011.0.00243.S, #2011.0.00319.S, #2011.0.00648.S, #2011.0.00767.S, #2012.1.00076.S, #2012.1.00602.S, #2012.1.00676.S, #2012.1.00719.S, #2012.1.00323.S, #2012.1.00536.S, #2012.1.00610.S, #2012.1.00934.S, and #2012.1.00953.S. ALMA is a partnership of ESO (representing its member states), NSF (USA) and NINS (Japan), together with NRC (Canada) and NSC and ASIAA (Taiwan), in cooperation with the Republic of Chile. The Joint ALMA Observatory is operated by ESO, AUI/NRAO and NAOJ. This work was supported by World Premier International Research Center Initiative (WPI Initiative), MEXT, Japan, and KAKENHI (23244025) and (15H02064) Grant-in-Aid for Scientific Research (A) through Japan Society for the Promotion of Science (JSPS).

REFERENCES

- Adelberger, K. L., Steidel, C. C., Giavalisco, M., et al. 1998, *ApJ*, 505, 18
- Adelberger, K. L., Steidel, C. C., Pettini, M., et al. 2005, *ApJ*, 619, 697
- Ashby, M. L. N., Stanford, S. A., Brodwin, M., et al. 2013, *ApJS*, 209, 22
- Austermann, J. E., Aretxaga, I., Hughes, D. H., et al. 2009, *MNRAS*, 393, 1573
- Austermann, J. E., Dunlop, J. S., Perera, T. A., et al. 2010, *MNRAS*, 401, 160
- Baugh, C. M., Lacey, C. G., Frenk, C. S., et al. 2005, *MNRAS*, 356, 1191
- Berger, E., Zauderer, B. A., Chary, R.-R., et al. 2014, *ApJ*, 796, 96
- Bertin, E., & Arnouts, S. 1996, *A&A*, 117, 393
- Blain, A. W., Chapman, S. C., Smail, I., & Ivison, R. 2004, *ApJ*, 611, 725
- Blanc, G. A., Lira, P., Barrientos, L. F., et al. 2008, *ApJ*, 681, 1099
- Bouchet, P., Lequeux, J., Maurice, E., Prevot, L., & Prevot-Burnichon, M. L. 1985, *A&A*, 149, 330
- Bouwens, R. J., Illingworth, G. D., Franx, M., et al. 2009, *ApJ*, 705, 936
- Bouwens, R. J., Illingworth, G. D., Oesch, P. A., et al. 2015, *ApJ*, 803, 34
- Carniani, S., Maiolino, R., De Zotti, G., et al. 2015, *ArXiv e-prints*, arXiv:1502.00640
- Casey, C. M., Narayanan, D., & Cooray, A. 2014, *Phys. Rep.*, 541, 45
- Chapin, E. L., Pope, A., Scott, D., et al. 2009, *MNRAS*, 398, 1793
- Chapman, S. C., Blain, A. W., Smail, I., & Ivison, R. J. 2005, *ApJ*, 622, 772
- Chapman, S. C., Scott, D., Borys, C., & Fahlman, G. G. 2002, *MNRAS*, 330, 92
- Chen, C.-C., Cowie, L. L., Barger, A. J., et al. 2013, *ApJ*, 776, 131
- Chen, C.-C., Cowie, L. L., Barger, A. J., Wang, W.-H., & Williams, J. P. 2014, *ApJ*, 789, 12
- Chen, C.-C., Smail, I., Swinbank, A. M., et al. 2015, *ApJ*, 799, 194
- Coe, D., Benítez, N., Broadhurst, T., & Moustakas, L. A. 2010, *ApJ*, 723, 1678
- Condon, J. J. 1974, *ApJ*, 188, 279
- Coppin, K., Chapin, E. L., Mortier, A. M. J., et al. 2006, *MNRAS*, 372, 1621
- Coppin, K., Halpern, M., Scott, D., et al. 2008, *MNRAS*, 384, 1597
- Daddi, E., Cimatti, A., Renzini, A., et al. 2004, *ApJ*, 617, 746

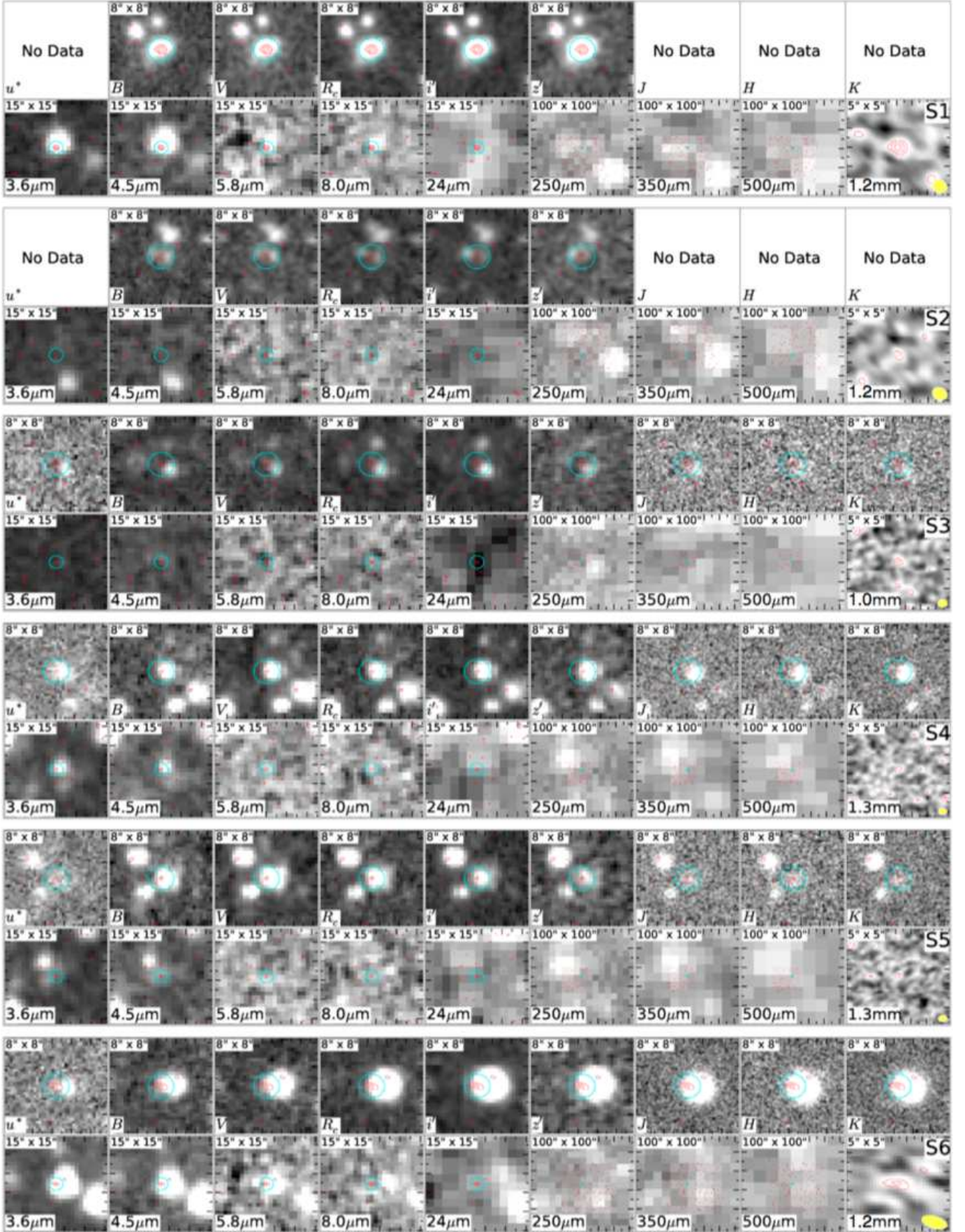


Figure 15. The snapshot images of the optical-NIR counterparts. The red contours indicate the ALMA mm band intensity at 2.4, 3.4, 4.4, and 5.4 σ levels. The cyan circle denotes the $1''$ search radius for the counterpart identifications. The wavelengths of the images range from 0.4 to 500 μm , which are shown with the labels in the images. The bottom right panels present the ALMA images with the beam sizes (yellow ellipses). In each panel, the size of the image is indicated. North is up, and east is to the left.

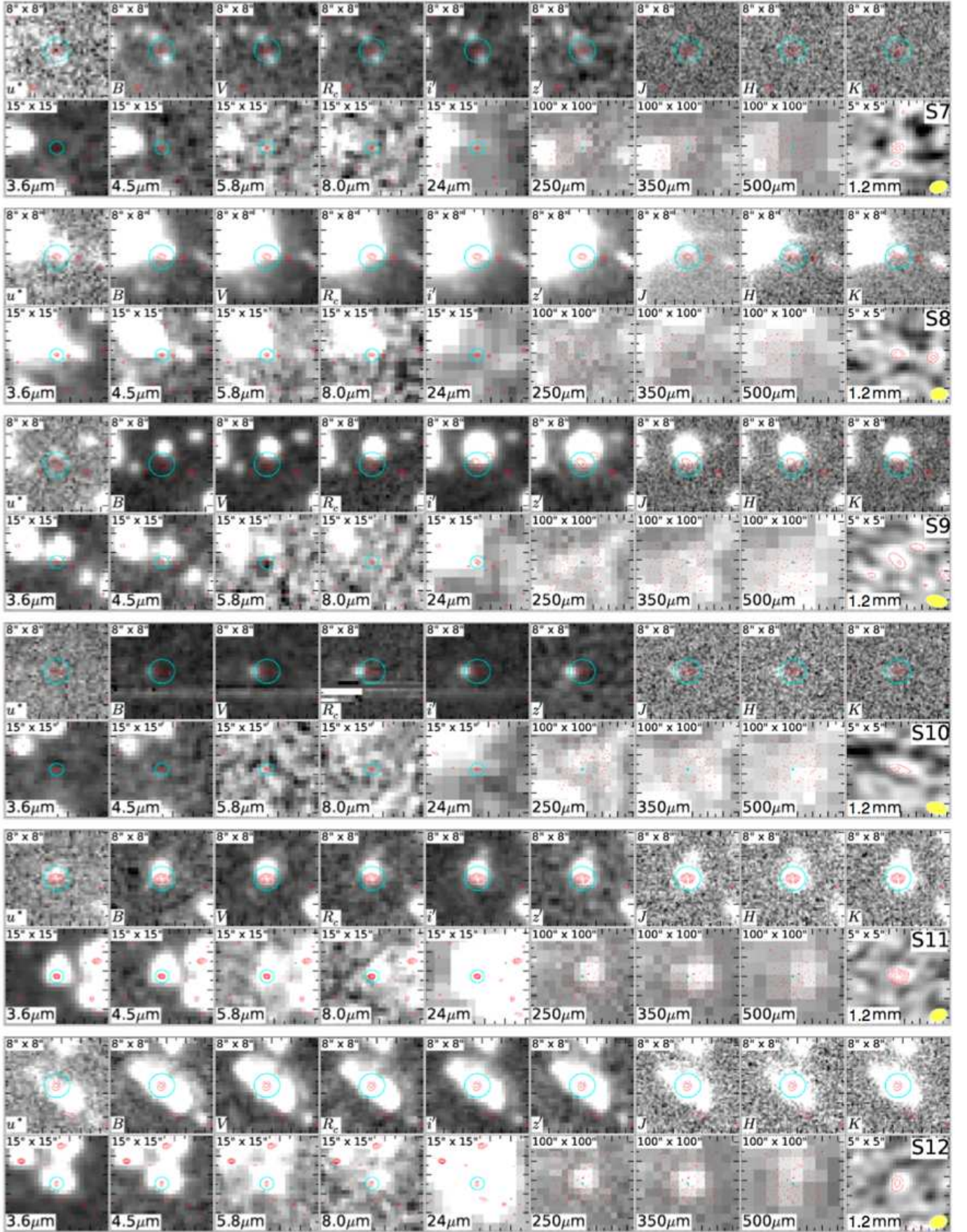


Fig. 15 (continued)

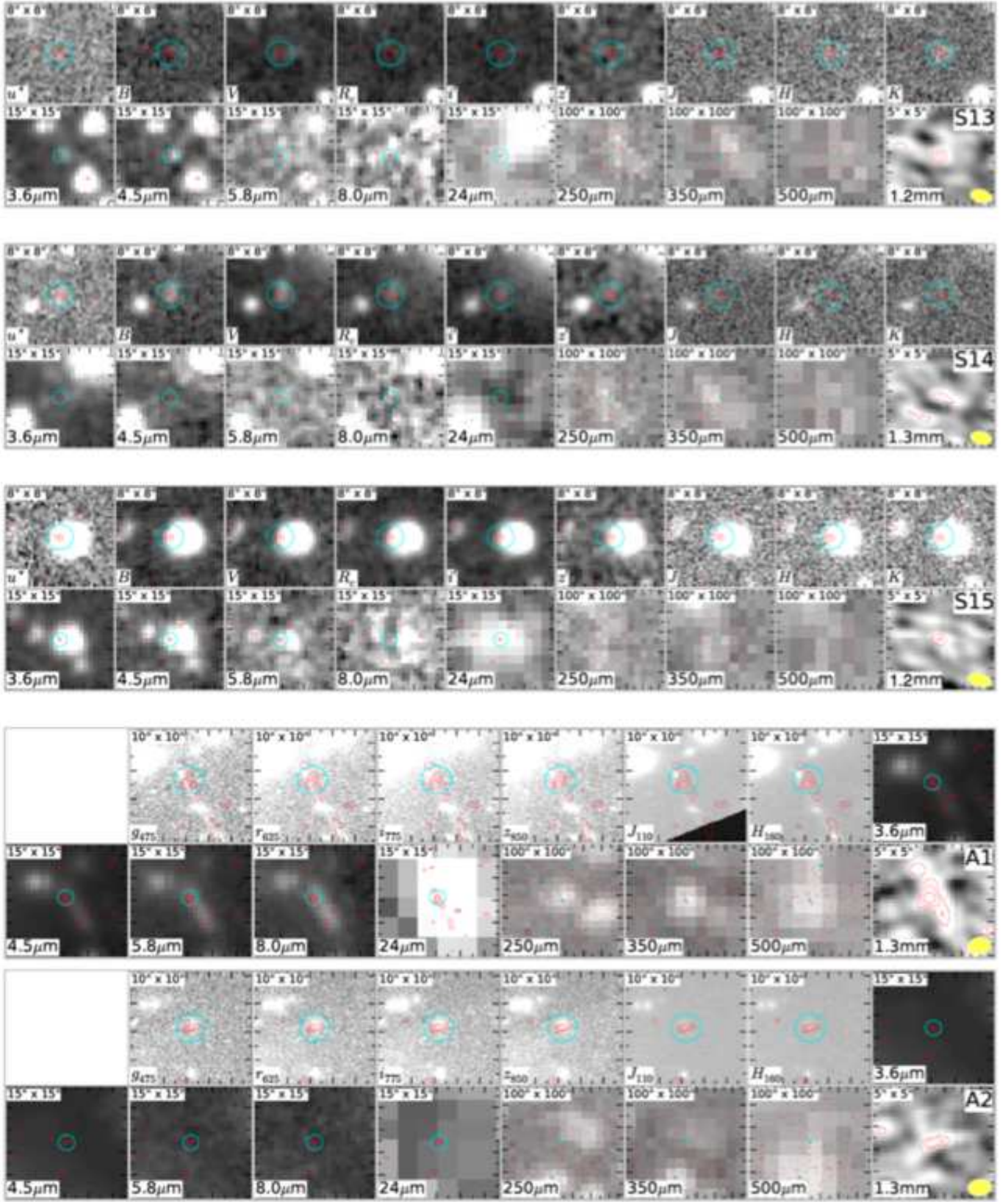


Fig. 15 (continued)

- Davies, L. J. M., Bremer, M. N., Stanway, E. R., & Lehnert, M. D. 2013, *MNRAS*, 433, 2588
- Decarli, R., Smail, I., Walter, F., et al. 2014, *ApJ*, 780, 115
- Diego, J. M., Broadhurst, T., Benitez, N., et al. 2015, *MNRAS*, 446, 683
- Dole, H., Lagache, G., Puget, J.-L., et al. 2006, *A&A*, 451, 417
- Downes, A. J. B., Peacock, J. A., Savage, A., & Carrie, D. R. 1986, *MNRAS*, 218, 31
- Eales, S., Lilly, S., Webb, T., et al. 2000, *AJ*, 120, 2244
- Fixsen, D. J., Dwek, E., Mather, J. C., Bennett, C. L., & Shafer, R. A. 1998, *ApJ*, 508, 123
- Fontanot, F., Monaco, P., Silva, L., & Grazian, A. 2007, *MNRAS*, 382, 903
- Fry, J. N. 1996, *ApJ*, 461, L65
- Furusawa, H., Kosugi, G., Akiyama, M., et al. 2008, *ApJS*, 176, 1
- Furusawa, J., Sekiguchi, K., Takata, T., et al. 2011, *ApJ*, 727, 111
- Gawiser, E., Francke, H., Lai, K., et al. 2007, *ApJ*, 671, 278
- Gehrels, N. 1986, *ApJ*, 303, 336
- Goldader, J. D., Meurer, G., Heckman, T. M., et al. 2002, *ApJ*, 568, 651
- Granato, G. L., De Zotti, G., Silva, L., Bressan, A., & Danese, L. 2004, *ApJ*, 600, 580
- Grazian, A., Fontana, A., Moscardini, L., et al. 2006, *A&A*, 453, 507
- Haberl, F., Motch, C., & Pietsch, W. 1998, *Astronomische Nachrichten*, 319, 97
- Hatsukade, B., Ohta, K., Endo, A., et al. 2014, *Nature*, 510, 247
- Hatsukade, B., Ohta, K., Seko, A., Yabe, K., & Akiyama, M. 2013, *ApJ*, 769, L27
- Hatsukade, B., Ohta, K., Yabe, K., et al. 2015, *ArXiv e-prints*, arXiv:1508.00644
- Hatsukade, B., Kohno, K., Aretxaga, I., et al. 2011, *MNRAS*, 411, 102
- Hauser, M. G., & Dwek, E. 2001, *ARA&A*, 39, 249
- Hauser, M. G., Arendt, R. G., Kelsall, T., et al. 1998, *ApJ*, 508, 25
- Hayashi, M., Shimasaku, K., Motohara, K., et al. 2007, *ApJ*, 660, 72
- Hayward, C. C., Narayanan, D., Kereš, D., et al. 2013, *MNRAS*, 428, 2529
- Hickox, R. C., Wardlow, J. L., Smail, I., et al. 2012, *MNRAS*, 421, 284
- Hodge, J. A., Karim, A., Smail, I., et al. 2013, *ApJ*, 768, 91
- Ikarashi, S., Ivison, R. J., Caputi, K. I., et al. 2014, *ArXiv e-prints*, arXiv:1411.5038
- Ishigaki, M., Kawamata, R., Ouchi, M., et al. 2015, *ApJ*, 799, 12
- Ivison, R. J., Greve, T. R., Serjeant, S., et al. 2004, *ApJS*, 154, 124
- Iye, M., Ota, K., Kashikawa, N., et al. 2006, *Nature*, 443, 186
- Johansson, D., Sigurdarson, H., & Horellou, C. 2011, *A&A*, 527, A117
- Karim, A., Swinbank, A. M., Hodge, J. A., et al. 2013, *MNRAS*, 432, 2
- Kennicutt, Jr., R. C. 1998, *ARA&A*, 36, 189
- Kneib, J.-P., van der Werf, P. P., Kraiberg Knudsen, K., et al. 2004, *MNRAS*, 349, 1211
- Knudsen, K. K., van der Werf, P. P., & Kneib, J.-P. 2008, *MNRAS*, 384, 1611
- Kochanek, C. S. 1991, *ApJ*, 373, 354
- Konno, A., Ouchi, M., Ono, Y., et al. 2014, *ApJ*, 797, 16
- Kovács, A., Chapman, S. C., Dowell, C. D., et al. 2006, *ApJ*, 650, 592
- Lagache, G., Puget, J.-L., & Dole, H. 2005, *ARA&A*, 43, 727
- Lee, K.-S., Alberts, S., Atlee, D., et al. 2012, *ApJ*, 758, L31
- Lee, K.-S., Giavalisco, M., Gnedin, O. Y., et al. 2006, *ApJ*, 642, 63
- Limousin, M., Richard, J., Jullo, E., et al. 2007, *ApJ*, 668, 643
- Lin, L., Dickinson, M., Jian, H.-Y., et al. 2012, *ApJ*, 756, 71
- Ly, C., Malkan, M. A., Hayashi, M., et al. 2011, *ApJ*, 735, 91
- Maiolino, R., Carniani, S., Fontana, A., et al. 2015, *ArXiv e-prints*, arXiv:1502.06634
- Makiya, R., Enoki, M., Ishiyama, T., et al. 2015, *ArXiv e-prints*, arXiv:1508.07215
- Martin, C. L., Sawicki, M., Dressler, A., & McCarthy, P. J. 2006, *New A Rev.*, 50, 53
- McMullin, J. P., Waters, B., Schiebel, D., Young, W., & Golap, K. 2007, *Astronomical Data Analysis Software and Systems XVI*, 127
- Meurer, G. R., Heckman, T. M., & Calzetti, D. 1999, *ApJ*, 521, 64
- Miller, T. B., Hayward, C. C., Chapman, S. C., & Behroozi, P. S. 2015, *ArXiv e-prints*, arXiv:1501.04105
- Mo, H. J., & White, S. D. M. 2002, *MNRAS*, 336, 112
- Oguri, M. 2010, *PASJ*, 62, 1017
- Oliver, S. J., Bock, J., Altieri, B., et al. 2012, *MNRAS*, 424, 1614
- Ono, Y., Ouchi, M., Kurono, Y., & Momose, R. 2014, *ApJ*, 795, 5
- Ota, K., Walter, F., Ohta, K., et al. 2014, *ApJ*, 792, 34
- Oteo, I., Zwaan, M. A., Ivison, R. J., Smail, I., & Biggs, A. D. 2015, *ArXiv e-prints*, arXiv:1508.05099
- Ouchi, M., Shimasaku, K., Okamura, S., et al. 2004, *ApJ*, 611, 685
- Ouchi, M., Shimasaku, K., Akiyama, M., et al. 2008, *ApJS*, 176, 301
- Ouchi, M., Mobasher, B., Shimasaku, K., et al. 2009, *ApJ*, 706, 1136
- Ouchi, M., Shimasaku, K., Furusawa, H., et al. 2010, *ApJ*, 723, 869
- Ouchi, M., Ellis, R., Ono, Y., et al. 2013, *ApJ*, 778, 102
- Overzier, R. A., Bouwens, R. J., Illingworth, G. D., & Franx, M. 2006, *ApJ*, 648, L5
- Peebles, P. J. E. 1993, *Principles of Physical Cosmology* (Princeton University Press)
- Perera, T. A., Chapin, E. L., Austermann, J. E., et al. 2008, *MNRAS*, 391, 1227
- Planck Collaboration, Abergel, A., Ade, P. A. R., et al. 2011, *A&A*, 536, A21
- Puget, J.-L., Abergel, A., Bernard, J.-P., et al. 1996, *A&A*, 308, L5
- Quadri, R., van Dokkum, P., Gawiser, E., et al. 2007, *ApJ*, 654, 138
- Reddy, N., Dickinson, M., Elbaz, D., et al. 2012, *ApJ*, 744, 154
- Robertson, B. E. 2010, *ApJ*, 716, L229
- Schechter, P. 1976, *ApJ*, 203, 297
- Scott, K. S., Wilson, G. W., Aretxaga, I., et al. 2012, *MNRAS*, 423, 575
- Scoville, N., Aussel, H., Brusa, M., et al. 2007, *ApJS*, 172, 1
- Scoville, N., Sheth, K., Aussel, H., et al. 2015, *ArXiv e-prints*, arXiv:1505.02159
- Sheth, R. K., & Tormen, G. 1999, *MNRAS*, 308, 119
- Shimizu, I., Yoshida, N., & Okamoto, T. 2012, *MNRAS*, 427, 2866
- Silva, A., Sajina, A., Lonsdale, C., & Lacy, M. 2015, *ApJ*, 806, L25
- Simpson, C., Martínez-Sansigre, A., Rawlings, S., et al. 2006, *MNRAS*, 372, 741
- Simpson, J. M., Swinbank, A. M., Smail, I., et al. 2014, *ApJ*, 788, 125
- Simpson, J. M., Smail, I., Swinbank, A. M., et al. 2015a, *ApJ*, 807, 128
- . 2015b, *ApJ*, 799, 81
- Smail, I., Ivison, R. J., Blain, A. W., & Kneib, J.-P. 2002, *MNRAS*, 331, 495
- Steidel, C. C., Adelberger, K. L., Shapley, A. E., et al. 2003, *ApJ*, 592, 728
- Steidel, C. C., Shapley, A. E., Pettini, M., et al. 2004, *ApJ*, 604, 534
- Swinbank, A. M., Smail, I., Longmore, S., et al. 2010, *Nature*, 464, 733
- Takeuchi, T. T., Yuan, F.-T., Ikeyama, A., Murata, K. L., & Inoue, A. K. 2012, *ApJ*, 755, 144
- Tanvir, N. R., Levan, A. J., Fruchter, A. S., et al. 2012, *ApJ*, 754, 46
- Trentham, N., Kormendy, J., & Sanders, D. B. 1999, *AJ*, 117, 2152
- Ueda, Y., Watson, M. G., Stewart, I. M., et al. 2008, *ApJS*, 179, 124
- Vanzella, E., Pentericci, L., Fontana, A., et al. 2011, *ApJ*, 730, L35
- Watson, D., Christensen, L., Kraiberg Knudsen, K., et al. 2015, *ArXiv e-prints*, arXiv:1503.00002
- Webb, T. M., Eales, S., Foucaud, S., et al. 2003, *ApJ*, 582, 6
- Weiß, A., Kovács, A., Coppin, K., et al. 2009, *ApJ*, 707, 1201
- Williams, C. C., Giavalisco, M., Porciani, C., et al. 2011, *ApJ*, 733, 92
- Williams, R. J., Quadri, R. F., Franx, M., van Dokkum, P., & Labbé, I. 2009, *ApJ*, 691, 1879
- Willott, C. J., Omont, A., & Bergeron, J. 2013, *ApJ*, 770, 13
- Willott, C. J., Delorme, P., Reyle, C., et al. 2010, *AJ*, 139, 906

Yabe, K., Ohta, K., Iwamuro, F., et al. 2012, PASJ, 64, 60
Yuma, S., Ohta, K., & Yabe, K. 2012, ApJ, 761, 19

Yun, M. S., Scott, K. S., Guo, Y., et al. 2012, MNRAS, 420, 957
Zampieri, L., Campana, S., Turolla, R., et al. 2001, A&A, 378, L5